AGU PUBLICATIONS

JGR

Journal of Geophysical Research: Solid Earth

RESEARCH ARTICLE
10.1002/2017JB014510

**Key Points:**
- Site-specific equation for the two most important hydrous defects in olivine
- Hydrous Ti is the most relevant defect in shallow upper mantle, whereas Si defects dominate at higher pressure
- The new equation constrains water incorporation in the subducting slab and the mantle wedge

**Supporting Information:**
- Supporting Information S1
- Data Set S1
- Data Set S2

**Correspondence to:**
J. A. Padrón-Navarta,
padron@gm.univ-montp2.fr

**Citation:**
Padrón-Navarta, J. A., & Hermann, J. (2017). A subsolidus olivine water solubility equation for the Earth's upper mantle. *Journal of Geophysical Research: Solid Earth*, *122*. https://doi.org/10.1002/2017JB014510

Received 1 JUN 2017
Accepted 12 NOV 2017
Accepted article online 16 NOV 2017





# A Subsolidus Olivine Water Solubility Equation for the Earth's Upper Mantle

**J. A. Padrón-Navarta[1] and J. Hermann[2,3]**

[1]Géosciences Montpellier, CNRS and University of Montpellier, Montpellier, France, [2]Research School of Earth Sciences, Australian National University, Canberra, ACT, Australia, [3]Department of Geological Sciences, University of Bern, Bern, Switzerland

**Abstract** The pressure and temperature sensitivity of the two most important point hydrous defects in mantle olivine involving Si vacancies (associated to trace amounts of titanium [TiChu-PD] or exclusively to Si vacancies [Si]) was investigated at subsolidus conditions in a fluid-saturated natural peridotite from 0.5 to 6 GPa (approximately 20–200 km depth) at 750 to 1050°C. Water contents in olivine were monitored in sandwich experiments with a fertile serpentine layer in the middle and olivine and pyroxene sensor layers at the border. Textures and mineral compositions provide evidence that olivine completely recrystallized during the weeklong experiments, whereas pyroxenes displayed only partial equilibration. A site-specific water solubility law for olivine has been formulated based on the experiments reconciling previous contradictory results from low- and high-pressure experiments. The site-specific solubility laws permit to constrain water incorporation into olivine in the subducting slab and the mantle wedge, as these are rare locations on Earth where fluid-present conditions exist. Chlorite dehydration in the hydrated slab is roughly parallel to the isopleth of 50 ± 20 ppm wt $H_2O$ in olivine, a value which is independent of the pressure and temperature trajectory followed by the slab. Hydrous defects are dominated by [Si] under the relevant conditions for the mantle wedge affected by fluids coming from the slab dehydration (slab-adjacent low viscosity/seismic low-velocity channel, $P > 3$ GPa). In cold subduction zones at 5.5 km from the slab surface the storage capacity of the mantle wedge at depths of 100–250 km ranges from 400 to 2,000 ppm wt $H_2O$.

## 1. Introduction

Plate tectonics causes the largest recycling system on Earth, but the extent to which volatiles are coupled to this cycle is uncertain (e.g., Demouchy & Bolfan-Casanova, 2016; Hirschmann, 2006; Peslier et al., 2017). Although the potential existence of water reservoirs in the Earth's mantle transition zone has been intensively investigated since the early experiments of Ringwood and Major (1967), its confirmation by means of geophysical observations is still a matter of debate. The recent discovery of hydrous ringwoodite trapped in ultradeep diamonds from the Earth's transition zone provides evidence that water might reach at least locally depths of 410–660 km (Pearson et al., 2014). Recent experiments suggest that the potential reservoirs might be further extended even deeper, at lower mantle conditions (e.g., Walter et al., 2015).

The transfer of volatiles from the hydrosphere to the mantle occurs through hydration (mostly serpentinization) and subduction of oceanic lithosphere (e.g., Hacker, 2008) and/or by transferring part of the fluid to the mantle wedge in contact with the subducting interface as a consequence of slab dehydration (also known as "seismic low-velocity channel," Iwamori, 2007; or "low viscosity channel," Hebert et al., 2009; Hebert & Montési, 2013). Constraining this flux is extremely challenging because of the combined uncertainty in (1) the extent of lithosphere hydration, (2) the thermal regime of subduction zones, and ultimately (3) the identification of the water carrier phases and their storage capacity. Early studies identified hydrous phases such as dense hydrous magnesium silicates or the 10 Å phase (with several wt % of equivalent $H_2O$ as structurally bounded OH groups) as the deepwater carrier phases in cold subduction zones (e.g., Fumagalli & Poli, 2005; Iwamori, 2007). However, recent numerical models advocate warmer slab temperatures, restricting water transport by these hydrous phases to the deeper and thus less hydrated parts of the subducted slab (van Keken et al., 2011). It is generally accepted that complete dehydration of the hydrated lithosphere occurs between 100 and 200 km in depth (approximately 3–6 GPa) at temperatures in the range of 600 to 800°C (Arcay et al., 2005; van Keken et al., 2011). The only alternative for deepwater transport is then through

nominally anhydrous minerals (NAMs) where hydrogen is incorporated as complex point defects in the mineral structure at the level of part per million of equivalent $H_2O$.

Extensive experimental studies have demonstrated that olivine can incorporate substantial amounts of hydrous point defects (e.g., Férot & Bolfan-Casanova, 2012; Kohlstedt et al., 1996). However, current experimental data on water solubility in NAMs cannot be extrapolated to the critical region in the slab at 100–200 km depth where most dehydration reactions are taking place at temperatures lower than 800°C (Schmidt & Poli, 1998). The vast majority of previous experiments in olivine have been conducted in simple systems at supersolidus conditions (typically in the range of 1100–1500°C) or at pressures believed to be close to supercritical conditions of the fluid phase (e.g., Ardia et al., 2012; Bali et al., 2008; Férot & Bolfan-Casanova, 2012; Kohlstedt et al., 1996; Mosenfelder et al., 2006; Sokol et al., 2010; Withers & Hirschmann, 2008; Withers et al., 2011). At these extreme conditions the chemical potential of water (i.e., water fugacity) cannot be directly constrained by using an equation of state for pure $H_2O$ due to the increase of the mineral solubility in the coexisting fluid/melt (e.g., Bali et al., 2008; Hermann et al., 2006). This precludes precise extrapolations from the previously experimentally investigated regions to lower temperature and pressure conditions where fluids are expected to be nearly pure $H_2O$. The experimental investigation of water incorporation into olivine at conditions encountered in the slab and the mantle wedge is particularly relevant, as these are rare locations on Earth where fluid-present conditions exist, allowing the direct application of water-saturated experiments to nature.

Hydrogen can be incorporated into the olivine structure through different mechanisms involving different types of vacancies (e.g., Ingrin et al., 2013; Mackwell & Kohlstedt, 1990) and/or coupled to other trace elements (Berry et al., 2005, 2007). In particular, titanium is considered to enhance water incorporation in olivine (Berry et al., 2005, 2007; Faul et al., 2016; Hermann et al., 2005; Walker et al., 2007), although recent experimental works (Gaetani et al., 2014) failed to constrain such correlation. Unfortunately, the pressure-temperature sensitivity of each of these hydrous defects and their sensitivity to trace elements remains unknown. Constraining these dependencies is essential to resolve conflicting views of the actual site where hydrogen is incorporated and to constrain partitioning between different hydrous defects at different conditions (Berry et al., 2007; Ingrin et al., 2013; Matveev & Stachel, 2007; Smyth et al., 2006; Walker et al., 2007). Furthermore, the incorporation of hydrogen into the olivine structure has been proposed to produce significant rheological weakening (Demouchy et al., 2012; Mackwell et al., 1985; Mei & Kohlstedt, 2000; Tielke et al., 2017) with potential implications for upper mantle rheology in fluid-rich settings such as subduction zones. More specifically, hydrous defects associated to silicon vacancies are believed to modify the diffusivity of the slowest element in olivine (i.e., Si) and therefore induce weakening in the diffusion creep (Costa & Chakraborty, 2008) and dislocation creep regime (Girard et al., 2013; Tielke et al., 2017). Recent experimental studies, however, strongly disagree not only in the extent to which upper mantle rheology is sensitive to hydrogen incorporation but also in the point defect mechanism responsible for the weakening (Demouchy et al., 2012; Faul et al., 2016; Fei et al., 2013; Tielke et al., 2017).

In order to investigate these issues, we have undertaken piston cylinder experiments in a complex natural peridotite system from 0.5 to 6 GPa (corresponding to approximately 20–200 km depth) in a temperature range never explored so far (from 750 to 1050°C) that are typical for the subducted slab and the mantle wedge. A site-specific water solubility law for olivine is deduced from thermodynamic assessment of the reactions leading to water incorporation into olivine. This new solubility equation can be applied to better constrain water recycling in subduction zones and will assist in constraining the rheology of the lithospheric mantle.

## 2. Experimental Strategy

We conducted a series of constant pressure experiments (from 750 to 1050°C with 50°C intervals at 3.0 GPa) and constant temperature experiments (from 0.5 to 6.0 GPa with 1.0 GPa intervals at 950°C, respectively) in addition to one experiment at 1.6 GPa and 710°C resulting in a total of 20 runs (Figure 1 and Table 1). We have modified the sensor layer technique of Kovács et al. (2012) by using a natural serpentinite as the water source layer in order to reproduce closely subduction zone processes. Mineral separates from two high-pressure metaperidotites (i.e., dehydrated serpentinites) were used as sensor layers. Phase assemblages in the dehydrated layer are shown in Figure 1 and Table 1.

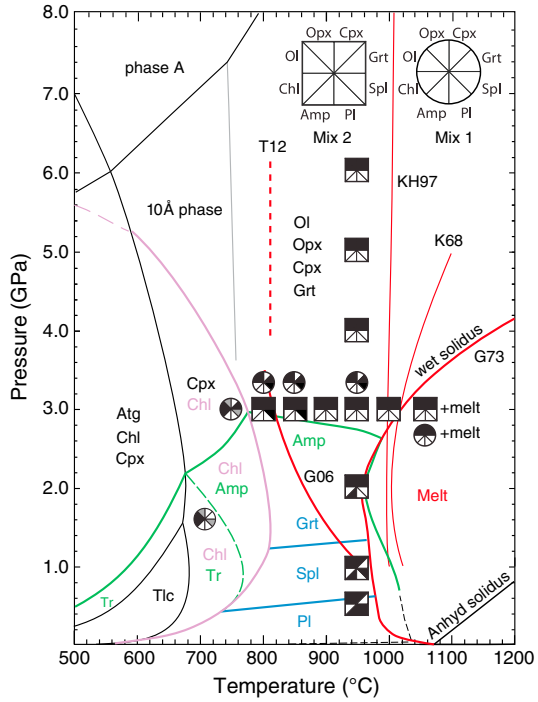


**Figure 1.** Experimental conditions investigated (see also Table 1) compared to the stability of hydrous phases (modified from Schmidt & Poli, 1998; Fumagalli & Poli, 2005): antigorite (Atg), talc (Tlc), and phase A (black lines), tremolite and amphibole/pargasite (Amp, green lines, maximum thermal stability field after Green, 1973, pyrolite +6 wt % $H_2O$), chlorite (Chl, purple line), and 10 Å phase (gray lines). Also shown are some wet solidi in red: T12 (Till et al., 2012), K68 (Kushiro et al., 1968), KH97 (Kawamoto & Holloway, 1997), G73 (Green, 1973), and G06 (Grove et al., 2006). Circles and squares using Mix 1 (serpentinite +1 wt % garnet seeds) and Mix 2 (serpentinite +10 wt % garnet +10 wt % clinopyroxene) as water source layers respectively. Black symbol for spinel denotes spinel s.s. (950°C) or aluminum chromite whereas gray symbol denotes magnetite/Cr-magnetite (cf. Table 1). Gray symbol for Opx denotes the occurrence of (possibly metastable) low clinoenstatite in addition to orthoenstatite.

### 2.1. Starting Material and Piston Cylinder Experiments

Fresh pieces of an antigorite serpentinite including some magnetite (sample Al06-44) from Cerro del Almirez (CdA) SE Spain (orogenic peridotite, e.g., Padrón-Navarta et al., 2011, and references therein) were crushed and ground in an agate mortar under acetone. Garnet (in Mix 1) and garnet + clinopyroxene separates (in Mix 2) from Cima di Gagnone (CdG) garnet lherzolite, Swiss Alps (orogenic peridotite, e.g., Scambelluri et al., 2014), were added as seeds to the serpentine powder and then reground. These seeds enhance nucleation and increase the modal proportion of garnet and pyroxene/amphibole in the garnet peridotite resulting from antigorite and chlorite breakdown (Figure 1 and Table 1). Olivine ($Ol^{CdA}$) and orthopyroxene ($Opx^{CdA}$) separates (90–120 μm in size) from Cerro del Almirez (sample Al08-16, chlorite harzburgite, Padrón-Navarta et al., 2011) and olivine ($Ol^{CdG}$), orthopyroxene ($Opx^{CdG}$), clinopyroxene ($Cpx^{CdG}$), and garnet ($Grt^{CdG}$) separates (90–120 μm in size) from Cima di Gagnone (sample MG160, garnet lherzolite, Scambelluri et al., 2014) were used as sensor layers with Mix 1 or Mix 2 serpentinite layers resulting in 4 configurations (Figure 2 and Table 1). The modal proportion in the separates was estimated based on electron backscattered diffraction (EBSD) mapping on run products: Ol layer (90–95%), Opx layer (50–70%), Cpx layer (90%), and Grt layer (75%). Bulk water contents in the capsules (Table 1) relates to the amount of antigorite and ranges from 3.1 to 4.0 wt % $H_2O$ (estimated based on the measured weight of different layers and the water content of the source layer stored in antigorite.) No additional free water was added to the capsule.

Experiments were performed in 0.5 inch (12.7 mm) 200 T end-loaded piston cylinder apparatuses at the Research School of Earth Sciences, RSES (The Australian National University, ANU) using a vessel with a 32 mm length bore, employing pure NaCl, low friction assemblies. The temperature gradient within the capsule is estimated to be lower than 10–25°C. The use of gold capsules and the "dry" furnace assembly produces conditions close to the Ni-NiO transition, which is similar to the fayalite-magnetite-quartz buffer in the investigated temperature range (i.e., oxygen fugacity conditions representative of metaperidotites). Pressure was measured directly, converting the load in the cell to pressure for a low friction assembly and was kept constant during the experiments. No pressure corrections were applied because of the low friction behavior of the NaCl cells and the relatively long run durations. Pressure is thought to be accurate within ±0.1 GPa. Experiments conducted at 5.0 and 6.0 GPa were carried out using a 500 T Harwood ultrahigh pressure piston cylinder apparatus at the RSES (ANU, Australia). Escape of liquid (presumably water) with some bubbling was noted during piercing of the capsule after the experiment in the majority of the runs (Table 1), indicating fluid saturation (except probably for the runs above the wet solidus). Capsules were cut in half with a low-speed diamond saw (210 μm blade thickness). One half was mounted in epoxy and polished for electron probe microanalyzer (EPMA) and EBSD analyses; the other part was thinned and double polished for Fourier transform infrared spectroscopy (FTIR) analyses with thicknesses in the range from 70 to 170 μm.

### 2.2. Globar Source and Synchrotron-Based FTIR Microspectroscopy

Globar source infrared spectra were obtained in the sensor layers and in the starting material with a Bruker Tensor 27 spectrometer mounted with a Bruker Hyperion microscope supplied with a liquid nitrogen-cooled mercury cadmium telluride detector at the RSES (ANU). Measurements were acquired under transmission using unpolarized and polarized (KRS-5 polarizer) infrared light. A square aperture with an edge length of 40–60 μm was used. Spectra were recorded in the range of 600 to 5,500 $cm^{-1}$ by averaging 64 or 128 scans with a resolution of 4 $cm^{-1}$. The microscope stage was continuously flushed with dry air during

**Table 1**
*Experimental Conditions, Capsule Configuration, and Mineral Assemblage After Serpentine Dehydration*

| Run # | *P* (GPa) | *T* (°C) | Duration (h) | Water source[a] | Bulk $H_2O$[b] | Sensor layer | Sensor material[c] | Excess water[d] | Mineral assemblage[e] |
|---|---|---|---|---|---|---|---|---|---|
| D1522 | 1.6 | 710 | 336 | Mix 1 | 3.9 | II | CdA | y | Ol, Opx/Cen, Chl, and Mag[e] |
| C4383 | 3.0 | 750 | 120 | Mix 1 | 3.8 | I | CdG | y | Ol, Opx/Cen, Chl, Cr-Mag, and Grt |
| D1516 | 3.0 | 800 | 240 | Mix 2 | 3.1 | III | CdG | y | Ol, Opx, Cpx, Al-Chr, and Grt |
| D1518 | 3.0 | 800 | 240 | Mix 1 | 3.7 | I | CdG | y | Ol, Opx, Al-Chr, and Grt |
| C4354 | 3.0 | 850 | 168 | Mix 1 | 3.5 | I | CdG | ND | Ol, Opx, Al-Chr, and Grt |
| D1503 | 3.0 | 850 | 168 | Mix 2 | 3.4 | III | CdG | y | Ol, Opx, Cpx, Al-Chr, and Grt |
| C4432 | 3.0 | 900 | 168 | Mix 2 | 3.3 | IV | CdG | y | Ol, Opx, Cpx, and Grt |
| C4365 | 3.0 | 950 | 168 | Mix 1 | 3.8 | I | CdG | y | Ol, Opx, Al-Chr, and Grt |
| C4368 | 3.0 | 950 | 164 | Mix 2 | 3.3 | III | CdG | y | Ol, Opx, Cpx, and Grt |
| D1520 | 3.0 | 950 | 168 | Mix 1 | 4.0 | II | CdA | y | Ol, Opx, Cr-Spl, and Grt |
| C4433 | 3.0 | 1000 | 168 | Mix 2 | 3.3 | IV | CdG | y | Ol, Opx, Cpx, and Grt |
| C4372 | 3.0 | 1050 | 168 | Mix 1 | 3.7 | I | CdG | y | Ol, Opx, Cpx, Grt, and melt |
| C4378 | 3.0 | 1050 | 168 | Mix 2 | 3.1 | III | CdG | y | Ol, Opx, Cpx, Grt, and melt |
| D1533 | 0.5 | 950 | 96 | Mix 2 | 3.3 | IV | CdG | y | Ol, Opx, Cpx, Spl, Amp, and Pl |
| D1527 | 1.0 | 950 | 96 | Mix 2 | 3.4 | IV | CdG | n | Ol, Opx, Cpx, Spl, and Amp |
| C4430 | 1.0 | 950 | 168 | Mix 2 | 3.1 | IV | CdG | y | Ol, Opx, Cpx, Spl, and Amp |
| D1523 | 2.0 | 950 | 152 | Mix 2 | 3.4 | IV | CdG | n | Ol, Opx, Cpx, Grt, and Amp |
| C4426 | 4.0 | 950 | 168 | Mix 2 | 3.4 | IV | CdG | y | Ol, Opx, Cpx, and Grt |
| UHPPC233 | 5.0 | 950 | 168 | Mix 2 | 3.3 | IV | CdG | n | Ol, Opx, Cpx, and Grt |
| UHPPC242 | 6.0 | 950 | 96 | Mix 2 | 3.1 | IV | CdG | y | Ol, Opx, Cpx, and Grt |

[a]Central layer: Mix 1 (serpentinite from Cerro del Almirez Al06-44 + 1 wt % garnet seeds), Mix 2 (Al06–44 + 10 wt % garnet + 10 wt % clinopyroxene seeds). All seeds are from Cima di Gagnone separates. [b]In wt % computed based on the relative amount of the water source layer (Mix 1 or Mix 2) and its composition. [c]Separates used in the sensor layer: CdG Cima di Gagnone and CdA Cerro del Almirez. [d]Escape of liquid (presumably water) with some bubbling was noted during piercing of the capsule after the experiment. ND, not determined. [e]All symbols are after Whitney and Evans (2010). Cen is low clinoenstatite $P2_1/c$ and chrome-Spl is picotite. [f]In addition to Mag a Ti-rich magnetite was also observed in this run.

measurement. The atmospheric compensation tool and background subtraction using the concave rubber band algorithm with three iterations of the OPUS® software was used after acquisition. Some spectra containing fluid inclusions were corrected by subtracting the broadband centered at approximately 3,440 $cm^{-1}$ by using a reference spectrum obtained for garnet + fluid inclusions where hydroxyl concentration was below the detection limit for the measured thickness.

The water content of fine-grained newly formed olivine after antigorite dehydration in the water source layer (Figure 2) on two selected runs was additionally measured by synchrotron radiation FTIR microspectroscopy in the beamline ID21 at the European Synchrotron Radiation Facility, Grenoble (France). Measurements were obtained with a Thermo Nicolet Nexus spectrometer mounted with Thermo Continuum microscope. Experimental conditions were 128 scans, resolution 4 $cm^{-1}$ and a squared aperture of 10 μm edge length.

The average of the unpolarized absorbance for a population of randomly oriented grains (typically between 10 and 20, Table 2) was used to quantify the water related to hydroxyl groups in NAMs following the approach of Kovács et al. (2008) for weakly absorbent anisotropic minerals. In this approach the average unpolarized absorbance approximates to one third of the total absorbance (i.e., sum of the absorbance along the three principal directions). Polarized absorbance in the most water-rich sample (Figure 3) never exceeds 0.2 units and therefore is in the application range for unpolarized measurements recommended by Kovács et al. (2008) having an estimated error of $<10\%$ in the total absorbance.

### 2.3. EBSD and EPMA

Phase assemblages in the dehydrated serpentinite layers (Table 1 and Figure 1) were investigated by means of high-resolution electron backscattered diffraction (EBSD) mapping obtained using a CamScan Crystal Probe X500-FEG with 15 keV acceleration voltage, 25 mm working distance, 2 Pa chamber pressure, and grid steps of 0.6–3 μm at Géosciences Montpellier (CNRS and University of Montpellier, France). Mineral compositions in sensor and in the water source layers (dehydrated serpentinite) were measured using a CAMECA SX100 microprobe. Analyses were carried out using an accelerating voltage of 15 keV and a beam current of 40 nA. Titanium ($TiO_2$ used as standard) was measured using two spectrometers (bPET and bLLIF) for 40 and 30 s, respectively, resulting in a detection limit of 140 ppm wt Ti (~220 ppm wt $TiO_2$).

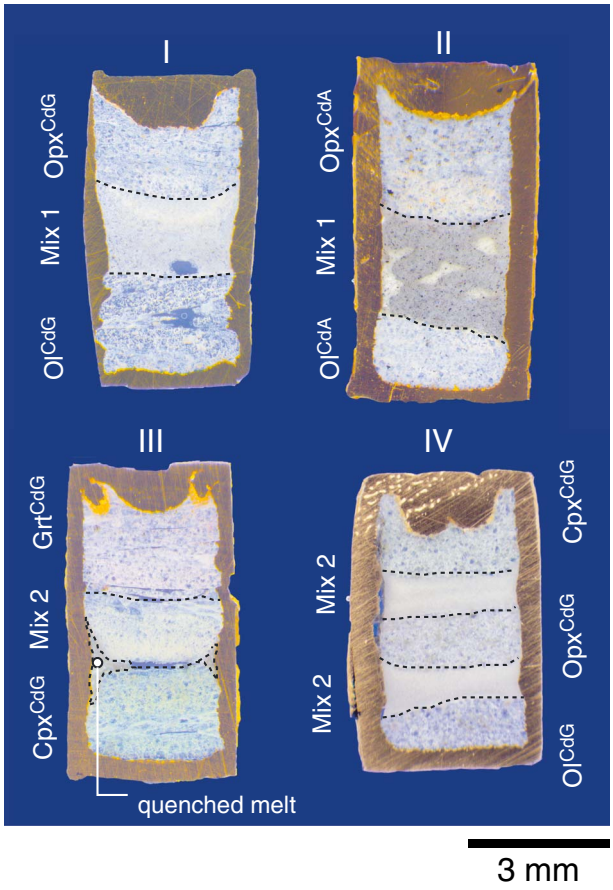


**Figure 2.** Examples of double-polished thick sections (from gold capsules) of the four configurations of sensor and water source layers (Mix 1 and Mix 2 = antigorite serpentinite, then transformed to metaperidotite at running conditions) used in this study (cf. Table 1). Starting material from Cima di Gagnone (CdG) and Cerro del Almirez (CdA) are mineral separates with 90–120 μm in size. The example for configuration III (run C4378, 3 GPa/1050°C) shows textures located close to the wall of the central part of the capsule that are interpreted as quenched hydrous melt.

## 3. Results

### 3.1. Phase Relations

Phase relations in the dehydrated serpentine layer (i.e., water source layer, Figure 1) are in agreement with previous experimental studies (e.g., Fumagalli & Poli, 2005; Schmidt & Poli, 1998). Amphibole (pargasite) is lacking at $P \geq 3$ GPa in agreement with its maximum pressure stability field in K-free systems (e.g., Green et al., 2010). Garnet occurs in all runs except at 1.0 GPa and 0.5 GPa (950°C), where the Al-rich phase is spinel and plagioclase ($An_{97}Ab_{03}$), respectively, and at 1.6 GPa/710°C where chlorite is stable. Magnetite occurs below 750°C, whereas at higher temperature it is transformed to Al-chromite or Cr-spinel (3 GPa, 800–950°C) and to spinel s.s. (0.5–1.0 GPa, 950°C). Pockets of dendritic material close to the wall capsule around the water source layer occur only in the two runs at 1050°C and 3 GPa (Figure 2 and Table 1). These pockets are interpreted as quenched hydrous melt, in agreement with the wet solidus proposed by Green (1973), Kushiro et al. (1968), and Kawamoto and Holloway (1997).

### 3.2. Water Content in Nominally Anhydrous Minerals (NAMs)

#### 3.2.1. Olivine

Olivine infrared spectra are dominated by absorbance at high wave number ($3{,}620 > \upsilon > 3{,}450$ cm$^{-1}$). Detailed polarized and unpolarized observations reveal the consistent occurrence of up to 11 peaks in this region (Figure 3a, 4, and 5). Most peaks are preferentially polarized along the [100] direction with the notable exception of peak 3 (3,581 cm$^{-1}$) and 5 (3,566 cm$^{-1}$), which show absorbance also, parallel to the [010] and [001], respectively (Figure 3). The position and polarization directions of peaks 1–3, 5, 6b, 7, and 9–11 (Figures 3–5) correspond to the ones described originally by Lemaire et al. (2004) (see also Ingrin et al. 2013, Figure 1 in Bali et al., 2008, and Table 1 in Padrón-Navarta et al., 2014) and are interpreted as being related to Si vacancies (labeled in the following as [Si], $(4H)^{x}_{Si}$ in Kröger-Vink notation). Peaks 4, 6a, and 8 correspond to those of Berry et al. (2005) (see also Jollands et al., 2016; Padrón-Navarta et al., 2014; Walker et al., 2007) and are interpreted as hydroxyl groups associated with $Ti^{4+}$ (the "Ti-clinohumite point defect," labeled here as [TiChu-PD] or in Kröger-Vink notation as $\left\{\left(Ti^{4+}\right)^{\bullet\bullet}_{Mg}\left(2H\right)^{''}_{Si}\right\}$). Water content in this study has been determined by fitting the complex spectra using the OPUS® peak fit tool, assuming a Gaussian distribution and fixing the peak position based on the whole data set. The summed average integrated absorbance of the two families of peaks ([Si] and [TiChu-PD]) in addition to the one related to trivalent defects, $[triv] = \left\{\left(Me^{3+}\right)^{\bullet}_{Mg}\left(H\right)^{'}_{Mg}\right\}$, are given in Tables 2 and 3 (see also Table S1 in the supporting information). Qualitatively, there is an excellent agreement between the fitted peaks derived from this study for [TiChu-PD] with 3,572 and 3,525 cm$^{-1}$ as main peaks (red in Figure 4) with experimental (Berry et al., 2005; Jollands et al., 2016) and natural olivine from spinel peridotites (e.g., San Carlos olivine, Schmädicke et al., 2013; Turner et al., 2015). The fitting peaks are also in agreement for [Si] peaks with main bands at 3,612, 3,581, and 3,566 cm$^{-1}$ (blue spectra in Figure 4) compared to synthetic (Bali et al., 2008; Férot & Bolfan-Casanova, 2012; Lemaire et al., 2004; Mosenfelder et al., 2006; Padrón-Navarta et al., 2014; Tollan et al., 2017; Withers et al., 2011) and olivine from some kimberlitic xenoliths (e.g., Doucet et al., 2014). Additionally, peak assignments are also in agreement with theoretical works based on first-principles calculations (e.g., Blanchard et al., 2017). It is worth noting that peak 2 (and possibly peaks 9 and 11) occur only in iron-bearing systems (compare the forsterite spectrum from Padrón-Navarta et al., 2014, in Figure 4 to the others and Blanchard et al., 2017, their Figure 1). Water measurements derived using polarized ($Abs_{tot}$) and unpolarized light (3 times the average unpolarized absorbance, $3 \cdot Abs_{avg}$,

AGU Journal of Geophysical Research: Solid Earth 10.1002/2017JB014510

**Table 2**

*Average (Unpolarized)/Integrated Absorbance ($cm^{-2}$) of Hydroxyl Stretching Bands and Water Concentration $C_{OH}$ (wt ppm $H_2O$) for Olivine, Orthopyroxene, Clinopyroxene, and Garnet in the Experiments and in the Starting Material*

| Run | *T* (°C) | *P* (GPa) | *t* (μm) | *n* | Average Abs ($cm^{-2}$) | | | $C_{H_2O}$ olivine[a] (wt ppm $H_2O$) | | $TiO_2$ (ppm wt %) | *t* (μm) | *n* | Average Abs ($cm^{-2}$) | | $C_{OH}$ opx[b] (wt ppm $H_2O$) | *t* (μm) | *n* | $C_{OH}$ cpx[b] (wt ppm $H_2O$) | $C_{OH}$ grt[b] (wtppm $H_2O$) |
|---|---|---|---|---|---|---|---|---|---|---|---|---|---|---|---|---|---|---|---|
| | | | | | [Si] | [TiChu-PD] | [triv] | B03 | W12 | | | | high *f* | low *f* | B95 | | | B95 | B95 |
| D1522 | 710 | 1.6 | 108(8) | 18 | 11 | 20 | 3 | 19 | 12 | 144(63) | 115(4) | 8 | 101 | b.d.l. | 20 | - | - | - | - |
| C4383 | 750 | 3.0 | 102(8) | 15 | 22 | 40 | 2 | 36 | 23 | 253(152) | 92(10) | 12 | 492 | b.d.l. | 99 | - | - | - | - |
| D1516 | 800 | 3.0 | - | - | - | - | - | - | - | 211(104) | - | - | - | - | - | 92(8) | 6 | 511 | b.d.l. |
| D1518 | 800 | 3.0 | 100(2) | 15 | 24 | 42 | 3 | 39 | 24 | 272(132) | 113(3) | 15 | 930 | 61 | 199 | - | - | - | - |
| C4354 | 850 | 3.0 | 119(3) | 13 | 64 | 80 | 2 | 82 | 52 | ND | 127(6) | 12 | 753 | 56 | 163 | - | - | - | - |
| D1503 | 850 | 3.0 | - | - | - | - | - | - | - | 464(194) | - | - | - | - | - | 96(3) | 12 | 602 | b.d.l. |
| C4432 | 900 | 3.0 | 130(2) | 10 | 79 | 102 | 4 | 105 | 66 | 358(204) | 117(6) | 10 | 880 | 54 | 188 | 90(2) | 10 | 816 | - |
| C4365 | 950 | 3.0 | 75(2) | 20 | 122 | 114 | 3 | 135 | 85 | 366(109) | 70(10) | 16 | 814 | 65 | 177 | - | - | - | - |
| C4365[c] | 950 | 3.0 | 75(2) | 23 | 151 | 110 | *3* | 149 | 94 | 366(109) | - | - | - | - | - | - | - | - | - |
| D1520[d] | 950 | 3.0 | 140(2) | 15 | 108 | 90 | 11 | 118 | 75 | 349(93) | 140(4) | 11 | 717 | 83 | 161 | - | - | - | - |
| C4368 | 950 | 3.0 | - | - | - | - | - | - | - | 423(120) | - | - | - | - | - | 88(3) | 18 | 816 | b.d.l. |
| C4433 | 1000 | 3.0 | 195(7) | 10 | 199 | 134 | 12 | 194 | 123 | 304(132) | 175(5) | 6 | 1,124 | 121 | 250 | 135(7) | 7 | 792 | - |
| C4372 | 1050 | 3.0 | 50(2) | 15 | 66 | 49 | 26 | 80 | 50 | 173(70) | 121(7) | 11 | 1,344 | 248 | 320 | - | - | - | - |
| C4378 | 1050 | 3.0 | - | - | - | - | - | - | - | 146(62) | - | - | - | - | - | 116(4) | 10 | 932 | b.d.l. |
| D1533 | 950 | 0.5 | 123(4) | 9 | 7 | 17 | 1 | 14 | 9 | 123(80) | 120(2) | 6 | 749 | 86 | 168 | 110(2) | 7 | 533 | - |
| D1527 | 950 | 1.0 | 80(2) | 11 | 15 | 33 | 3 | 28 | 18 | 213(107) | 80(2) | 7 | 664 | - | 133 | 70(10) | 8 | 808 | - |
| D4430 | 950 | 1.0 | 103(6) | 10 | 14 | 29 | 3 | 26 | 16 | 166(104) | 113(4) | 7 | 455 | 101 | 112 | 115(5) | 8 | 404 | - |
| D1523 | 950 | 2.0 | 38(3) | 9 | 52 | 62 | 5 | 67 | 43 | 276(147) | 91(10) | 7 | 749 | 86 | 168 | 126(11) | 8 | 836 | - |
| C4426 | 950 | 4.0 | 50(2) | 11 | 291 | 146 | 4 | 249 | 158 | 456(106) | 70(2) | 7 | 1,321 | 241 | 314 | 80(2) | 8 | 943 | - |
| UHPPC233 | 950 | 5.0 | 90(3) | 11 | 530 | 180 | 9 | 405 | 257 | 457(129) | 90(3) | 9 | 1,268 | 409 | 337 | 90(3) | 9 | 705 | - |
| UHPPC242 | 950 | 6.0 | 88(2) | 12 | 585 | 173 | 10 | 433 | 274 | 512(134) | 88(2) | 7 | 1,531 | 493 | 407 | 88(2) | 9 | 655 | - |
| UHPPC242[c] | 950 | 6.0 | 88(2) | 11 | 596 | 168 | *10* | 436 | 276 | 512(134) | 88(2) | 4 | 1,569[e] | 230[e] | 362 | - | - | - | - |
| Starting material[f] | | | | | | | | | | | | | | | | | | | |
| Al08–16 | - | - | 300(12) | 12 | 16 | 20 | b.d.l. | 20 | 13 | 115 | 300(12) | 9 | 7 | b.d.l. | 1 | - | - | - | - |
| MG160 | - | - | 335(14) | 23 | 19 | 36 | b.d.l. | 31 | 20 | 230 | 330(18) | 12 | 65 | 2 | 13 | 337(14) | 12 | 225 | 6[g] |

*Note*. ND, not determined. below detection limit (b.d.l.).

[a]B03 Bell et al. (2003) calibration, W12 Withers et al. (2012) calibration. The uncertainty in water content for olivine (shown in Figures 7 and 8) and other NAMs is estimated based on the uncertainty in the average unpolarized absorbance (10%) and in the calibration factor (15%) added in quadrature. [b]Integration range for opx: High-frequency range 3700–3200 $cm^{-1}$; low-frequency range 3,200–2,900 $cm^{-1}$, for cpx: 3,750–3,050 $cm^{-1}$, for grt: 3,750–3,450 $cm^{-1}$. [c]Newly formed olivine after antigorite breakdown from the source layer measured with synchrotron-based FTIR microspectroscopy. [d]The total water concentration for this run does not include the contribution of Mg vacancy, 19 $cm^{-2}$ (cf. Figure 5). [e]Opx free of fluid inclusions from the opx layer measured with synchrotron-based FTIR microspectroscopy. [f]The starting material also show minor peaks at approximately 3,400 $cm^{-1}$ related to lamellae of titanium clinohumite. Not included in the total water content. [g]Measured in a section with a thickness of 502(14) μm.

**Table 3**
*Total (Polarized) Integrated Absorbance ($cm^2$) of Hydroxyl Stretching Bands and Water Concentration COH (wt ppm $H_2O$) for Olivine*

| Run | T (°C) | P (GPa) | t (μm) | Total Abs ($cm^{-2}$)·1/3 | | | $C_{OH}$ Olivine (wt ppm $H_2O$) | | $TiO_2$ (ppm wt %) |
|---|---|---|---|---|---|---|---|---|---|
| | | | | [Si] | [TiChu-PD] | [triv] | B03 | W12 | |
| UHPPC242 | 950 | 6.0 | 88(2) | 512 | 173 | b.d.l. | 392 | 248 | 512(134) |

*Note.* Total absorbance is the sum of polarized measurements (*E//a* + *E//b* + *E//c*). For comparison with the average unpolarized measurements (Table 2) it is divided by 3.

Kovács et al., 2008) are qualitatively (Figures 3b and 3c) and quantitatively (Tables 2 and 3) similar within 15% relative error in agreement with other studies (e.g., Férot & Bolfan-Casanova, 2012; Tollan et al., 2017). Integrated total absorbance is transformed into water content using the calibrations of Bell et al. (2003) and Withers et al. (2012) (Tables 2 and 3).

Olivine infrared spectra for the OH-stretching region as a function of temperature and pressure from the sensor layers are shown in Figure 5 and Tables 2 and 3. Water contents steadily increase with temperature and pressure (Tables 2 and 3), but it can be clearly seen that [Si] and [TiChu-PD] behave differently. Peaks related to [TiChu-PD] are dominant at temperature lower than 850°C at 3 GPa and at pressure ≤ 2 GPa at 950°C, whereas peaks related to [Si] (e.g., see peak 1 at 3,612 $cm^{-1}$ in Figure 5) significantly increase with pressure (Figure 5) and to a lesser extent with temperature. The beginning of partial melting at 3 GPa results in a significant decrease in water content in both [Si] and [TiChu-PD] defects (from a total of 200 ppm wt $H_2O$ at 1000°C to 80 ppm at 1050°C, using B03 calibration). The peak related to trivalent cations (peak 12 at 3,353 $cm^{-1}$, $Fe^{3+}$; Berry et al., 2007) is subsidiary at all conditions except for the run with evidence of partial melting where another peak at 3,325 $cm^{-1}$ appears (most probably related to $Cr^{3+}$, Berry et al., 2007; Tollan et al., 2015). At the supersolidus conditions observed in this work (1050°C) the water content associated to trivalent cations represent approximately 20% of the total integrated absorbance but are negligible (<3%) at subsolidus conditions (Tables 2 and 3). The occurrence of two peaks (3,354 and 3,329 $cm^{-1}$) and a high proportion of trivalent defects were also reported by Kovács et al. (2012) at temperatures higher than 1000°C at 2.5 and 4.0 GPa. A minor contribution (<8% in total absorbance) of OH stretching associated to magnesium vacancies [Mg] = $(2H)^{x}_{Mg}$ (approximately 3,220 $cm^{-1}$) was only observed at 950°C and 3.0 GPa when using olivine from Cerro del Almirez as sensor layer.

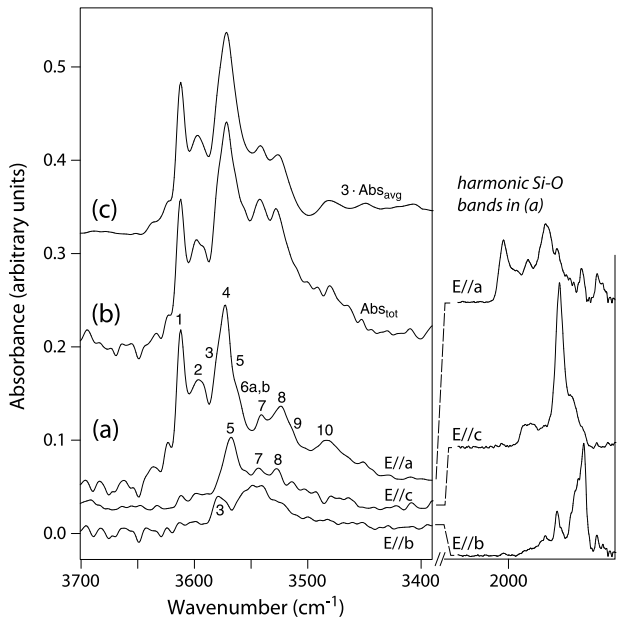


**Figure 3.** (a) Absorbance (not normalized to thickness) for olivine along the three principal directions ($A_a$, $A_b$, and $A_c$) shown in the inset on the right (harmonic Si-O stretching bands) using polarized IR light on two grains for the most water-rich sample found in this study (UHPPC242, 6 GPa/950°C). Note that most peaks are polarized parallel to the a-direction and are below 0.2 units. Numbers indicate identified O-H peaks (cf. Figures 4 and 5). (b) Total absorbance ($Abs_{tot} = A_a + A_b + A_c$) derived from polarized IR light measurements (corresponding to 392 ± 70 wt ppm $H_2O$, Bell et al., 2003 calibration). (c) Three times the average unpolarized absorbance for the same run ($3 \cdot Abs_{avg} = 3/n \sum Abs_i$, where *i* denotes the *i*th measurement with unpolarized light and *n* = 12 in this particular case, Table 2). Water content derived from $3 \cdot Abs_{avg}$ is 433 ± 78 wt ppm $H_2O$ and corresponds within the errors to those of Figure 3b.

Water content in olivine formed in the water source layer (Figure 2) after antigorite dehydration was also measured in two runs (C4365 and UHPPC242, Table 2) by synchrotron-based FTIR microspectroscopy, and it was found to be similar to those corresponding to the sensor layer (i.e., recrystallized starting material) within <15% relative difference.

### 3.2.2. Pyroxenes and Garnet

Orthopyroxene and clinopyroxene spectra significantly change quantitatively (Table 2) and qualitatively (Figure S1 in the supporting information) when compared to the starting sensor material. The main OH-stretching bands for orthopyroxene are: two broadbands at ~3,070 and ~3,420 $cm^{-1}$, two narrower and partially overlapping peaks at 3,515 and 3,545 $cm^{-1}$, and another relatively narrow peak at ~3,600 $cm^{-1}$. These bands are similar to those described by Kovács et al. (2012) using natural orthopyroxene sensor material (despite the higher $Al_2O_3$ content in their starting sensor orthopyroxene (2.83 and 6.30 wt %) compared to this study, <0.80 wt %) and those described by Férot and Bolfan-Casanova (2012) for the FMASH system below 5 GPa. Similar results were found by Demouchy et al.

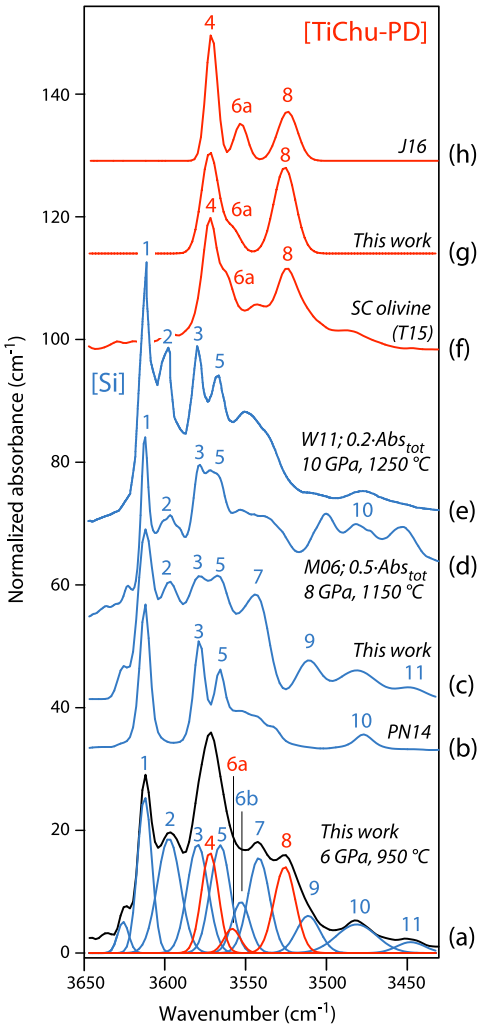


**Figure 4.** (a) An example of spectrum normalized to 1 cm thickness from this work (UHPPC242, cf. Figure 3) resolved into two groups of Gaussian distributions (bottom) corresponding to Si vacancies [Si] (in blue) and Ti-clinohumite point defect [TiChu-PD] (in red). Each family of peaks are summed separately (referred as "this work") and compared with other experimental and natural olivine multiplied by a scaling factor for better comparison: [Si] (in blue). (b) PN14: undoped MgO-buffered forsterite from Padrón-Navarta et al. (2014), multiplied by a factor of 0.5; (c) only [Si] peaks from spectrum in Figure 4a; (d) M06: recrystallized fine-grained Kilbourne Hole olivine (run ww227) from Mosenfelder et al. (2006) multiplied by a factor of 0.5; (e) W11: synthetic olivine in the FMSH system (run M475) from Withers et al. (2011) multiplied by a factor of 0.2; [TiChu-PD] (in red): (f) SC San Carlos olivine from Turner et al. (2015, their Figure 4) multiplied by a factor of 10; (g) only [TiChu-PD] peaks from spectrum in Figure 4a; (h) J16: annealed Ti-doped forsterite in the TiMSHO system partially hydroxilated from Jollands et al. (2016) multiplied by a factor of 13.

(2017), during annealing at subsolidus conditions. Interestingly at $P \geq 4$ GPa and 950°C a new peak appears at ~3,685 cm$^{-1}$ (Figure S2 in the supporting information, black triangles) that might correspond to high clinoenstatite (e.g., Withers & Hirschmann, 2007). Clinopyroxene shows a prominent peak at 3,640 cm$^{-1}$ and two broad minor peaks at ~3,450 and ~3,360 cm$^{-1}$ equivalent to those described by Kovács et al. (2012) and Demouchy et al. (2017).

Water contents of orthopyroxene observed in this study at 710°C and 750°C (<100 ppm wt $H_2O$) likely reflect an incomplete hydration of existing vacancies whereas the concentrations at $T$ 800–950°C up to 3 GPa (160–200 ppm wt $H_2O$) suggest fully hydration of available vacancies. At higher temperatures (1000–1050°C at 3 GPa) and $P \geq 4$ GPa, the corresponding higher water content (250–410 ppm wt $H_2O$) indicate partial reequilibration and creation of new vacancies (in agreement with the appearance of new peaks at $P \geq 4$ GPa, Figure S2 in the supporting information). A less clear trend is observed for clinopyroxene where the water content ranges from 500 to 900 wt ppm $H_2O$ (Tables 2 and 3). Water content in garnet from the experiments was always below the detection limit (supporting information Figure S3) for the investigated thickness (100–120 μm). An OH-stretching band at 3,570 cm$^{-1}$ in garnet was observed in the starting sensor material using a 500 μm thick section. The absorbance corresponding to this band is 6 ppm wt $H_2O$ (Table 2) using the calibration of Bell et al. (1995).

### 3.3. Mineral Chemistry

#### 3.3.1. Olivine

Titanium contents in newly formed and sensor layer olivine correlate with temperature and pressure departing from the composition of the original starting material (Figure 6). Titanium content in olivine from the garnet peridotite MG160 (Cima di Gagnone) used as starting sensor layer measured by laser ablation-inductively coupled plasma mass spectrometry (LA-ICPMS) ranges from 190 to 250 wt ppm (with two outliers at 27 and 880 wt ppm) having a median value of 230 wt ppm $TiO_2$ ($n$ = 22, Scambelluri et al., 2014). Olivine from chlorite-harzburgite (Cerro del Almirez, granofels texture) also used as starting sensor material (Table 1) has 115 ppm wt ppm $TiO_2$ (Marchesi et al., 2013). Olivine from Cima di Gagnone contains abundant oriented inclusions of ilmenite (Risold et al., 2003) with an average length of 10–20 μm and a cross section of 1 μm, whereas olivine from Cerro del Almirez contains lamellae of titanclinohumite (López Sánchez-Vizcaíno et al., 2005). Bulk LA-ICPMS data might potentially correspond to $TiO_2$ solubility concentrations previous to exsolution (Hermann et al., 2005). Average values above the detection limit obtained by EPMA are found at $T \geq 850$°C and $P \geq 3$ GPa (Figure 6). $TiO_2$ content in olivine from the sensor and the water source layer overlap given the uncertainty, independently of the olivine starting material (compare MG160 to Al08-16 at 3 GPa and 950°C in Figure 6). The apparent increase in $TiO_2$ content with temperature significantly drops when melt is present probably reflecting the preferential incorporation of Ti into melt. $TiO_2$ content increases with pressure up to 4 GPa. At higher pressure it is difficult to judge if $TiO_2$ reaches a constant value of 450 ± 100 wt ppm $TiO_2$, which is strikingly similar to the maximum value reported in the literature (Hermann et al., 2005).

#### 3.3.2. Pyroxenes and Garnet

Orthopyroxene formed after antigorite dehydration (water source layer, blue symbols in Figure 6) shows a significant variation in aluminum content with temperature and especially with pressure through a

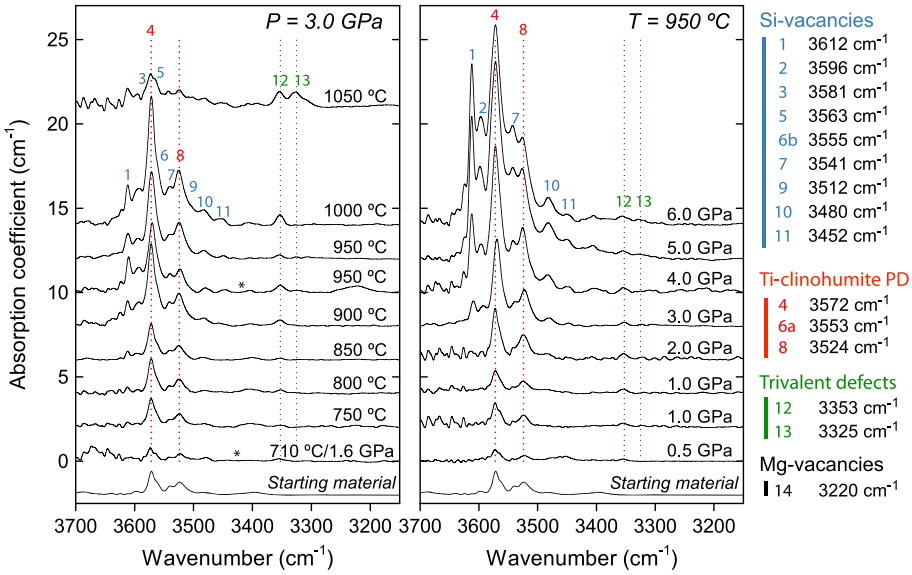


**Figure 5.** Olivine infrared OH stretching normalized to 1 cm thickness as a function of temperature at (left) 3 GPa and as a function of pressure at (right) 950°C. Asterisks indicate runs using Cerro del Almirez starting sensor material (Al08-16). Numbers from 1 to 14 indicate peak positions and are classified in four groups at the far right. Note that at pressure higher than 3 GPa [Si] starts to dominate. The apparent increase in absorbance around peak 4 at high-pressure results from the increase in absorbance of two overlapping peaks (3 and 5) from [Si]. The absorbance of [TiChu-PD] remains constant after 4 GPa but [Si] steadily increase (see Figure 8 and text for discussion).

Mg-Tschermaks exchange, in agreement with equilibrium modeling. In contrast, only orthopyroxene rims from the sensor layer change toward the equilibrium values, whereas most of the cores retain the composition of the starting material (gray band in Figure 6). Similarly clinopyroxene and garnet from the sensor layer fail to fully equilibrate compositionally toward predicted equilibrium values, despite relatively long run duration (~168 h, Table 1).

## 4. Discussion

### 4.1. Assessment of Equilibrium

One of the main experimental challenges encountered in the investigation of the water solubility in NAMs is the assessment of equilibrium given the different approaches and contrasting types of starting material previously used (e.g., coarse- and fine-grained natural powders, synthetic oxide powders, or large millimeter-size single crystal, see Kovács et al., 2012 for a comprehensive discussion). Five lines of evidence demonstrate that the olivine in the sensor layer from this study attained equilibrium. (I) Olivine commonly shows straight grain boundaries, abundant 120 triple junctions, and no internal deformation (see also Aradi et al., 2017). (II) The water concentration in olivine in the sensor layers is different from the starting material (Figure 5 and stars in Figure 7). (III) Two compositionally different starting olivines (CdG and CdA, Tables 2 and 3) produced identical spectra at 950°C, 3 GPa (Figure 5). (IV) There is good agreement between the spectra of olivine recrystallized from the sensor layer and the olivine formed after antigorite dehydration in the water source layer measured by synchrotron-based FTIR microspectroscopy. (V) Water contents in olivine in the sensor layer vary systematically with pressure and temperature (Figure 8).

Equilibration of the sensor layers can be achieved either by diffusion or recrystallization. Based on diffusion data for proton-vacancy exchange in olivine (Demouchy & Mackwell, 2006), the starting material used in this study would be fully hydroxylated (≥95%) after 168 h even at 750°C. Similar results are found for orthopyroxene (Stalder & Skogby, 2003), whereas mantle clinopyroxene and garnet should reequilibrate even faster (e.g., Ferriss et al., 2016). Recent experiments by Jollands et al. (2016) demonstrate, however, that this kind of hydroxylation using highly mobile proton-(magnesium) vacancy preserves metastable configuration of defects out of equilibrium from externally imposed silica activity or oxygen fugacity conditions. Therefore, hydroxylation does not guarantee the homogenization of all chemical potentials. Moreover, if, for instance, equilibrium defect concentrations in the present experiments were to be produced by extremely slow

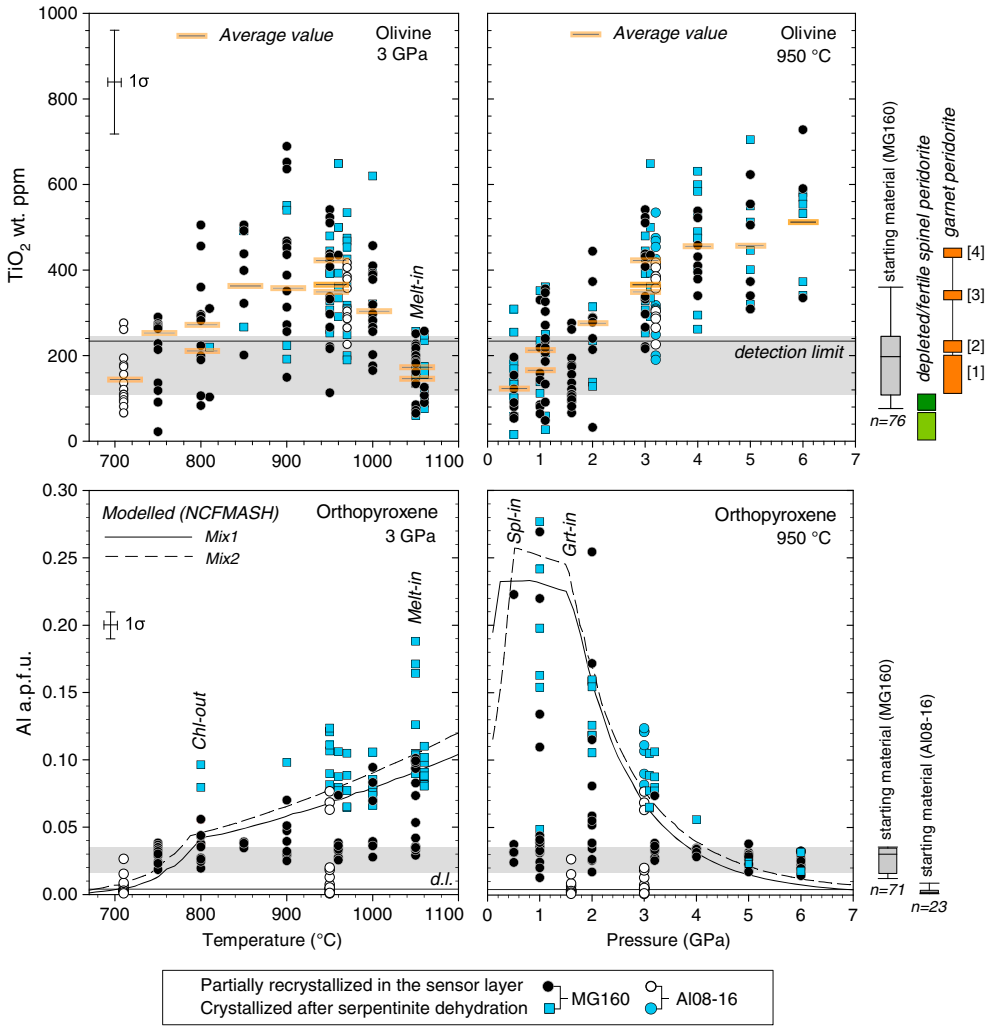


**Figure 6.** Temperature (at 3 GPa) and pressure (at 950°C) evolution of (top row) $TiO_2$ in olivine and (bottom row) aluminum in atoms per formula unit (a.p.f.u.) in the orthopyroxene. Most experiments refer to garnet peridotite sensor starting material (MG160). Blue colors indicate analyses on the crystallized material from the original water source layer (i.e., dehydrated serpentinite), whereas black and white colors indicate analyses of partially recrystallized crystals from the sensor layers (mineral separates). For comparison some $TiO_2$ concentrations in olivine reported in the literature is shown in Figure 6 (top right): depleted/fertile spinel peridotite from Hermann et al., 2005, and reference therein and Schmädicke et al., 2013; garnet peridotite [1]: Hermann et al., 2005, and reference therein; [2] LA-ICPMS of sample MG160 from Cima di Gagnone as given by Scambelluri et al. (2014); [3] Alpe Arami garnet peridotite (Hacker et al., 1997); and [4] maximum content reported by Hervig et al. (1986). The gray horizontal band shows the variability observed in the MG160 starting material (lower and upper limits are the 25th and 75th percentiles). Also shown for orthopyroxene is the modeled evolution of Al in a.p.f.u. with PerpleX (Connolly, 2009) for the dehydrated serpentinite (Mix 1 and Mix 2 continuous and dashed lines, respectively).

diffusion of proton-silicon vacancies [Si] (Padrón-Navarta et al., 2014), olivine hydroxylation would reach 90–95% of completion only at 1050°C. At 950°C these values will drop to only 25–35% and hydroxylation would be negligible at lower temperature. It is concluded that diffusion alone is unlikely to achieve the equilibration of the sensor layers, and thus, the most plausible alternative is olivine recrystallization by dissolution-precipitation mechanisms. This hypothesis is further supported by the 1:2 correlation between the titanium content in olivine and the amount of hydrogen linked exclusively to [TiChu-PD], that is, $MgTiH_2O_4$ (Tables 2 and 3 and Figures 6 and 7) when plotted in molar proportions (μmol/g). The data plot closer to the 1:2 correlation for the Bell et al. (2003) calibration than for the calibration of Withers et al. (2012) as has been noted also by Tollan et al. (2017).

Pyroxene and garnet in the sensor layer display abundant internal microstructures and subgrain boundaries are observed in pyroxenes probably produced by compaction and porosity collapse during the initial step of cold compression in the piston cylinder. The FTIR spectra of pyroxene in the sensor layers and water contents are different from the starting material (Table 2 and Figures S1 and S2 in the supporting information);

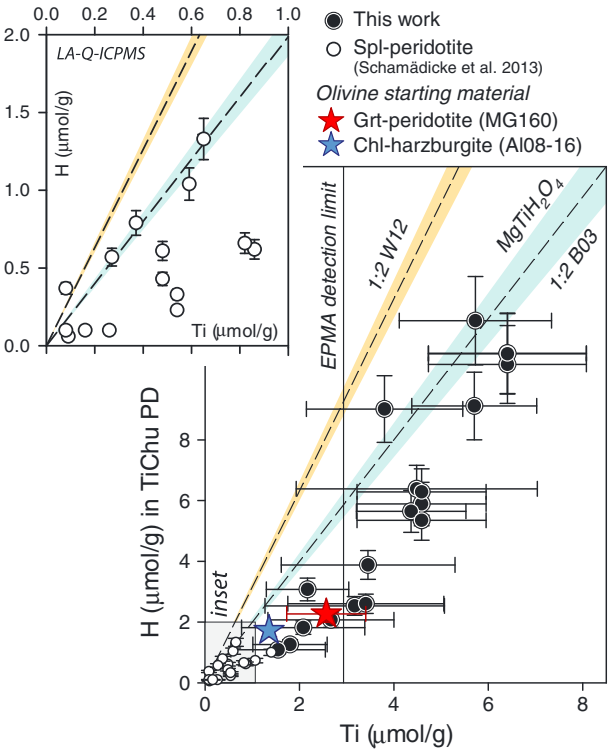


**Figure 7.** Hydrogen related exclusively to [TiChu-PD] (Bell et al., 2003 calibration) versus titanium in μm/g from the present experiments (Tables 2 and 3) measured by EPMA, the two starting materials measured by LA-ICPMS (red and blue starts, Scambelluri et al., 2014 and Marchesi et al., 2013, respectively) and data obtained by means of LA-Q-ICPMS for some spinel peridotites (inset, Schmädicke et al., 2013). For comparison the relative position of the 1:2 if the calibration of Withers et al. (2012) is also shown. Note that abundant inclusions of ilmenite rods in MG160 olivine (red star) are observed, therefore contributing to its bulk Ti content.

however, water contents do not vary systematically with pressure and temperature. Additionally, the compositions of pyroxene and garnet do not change in the sensor layers and they are different from the newly grown pyroxenes in the peridotite that results from serpentine dehydration (Figure 6). All these observations suggest that during the experiments only hydration of preexisting defects (Jollands et al., 2016) but no extensive recrystallization of pyroxenes occurred. Therefore, the following discussion will be based solely on water contents in olivine.

### 4.2. Site-Specific Water Solubility Law for Olivine: Linking Low- to High-Pressure Experiments

Results from this study suggest that hydrous defects in olivine behave differently with temperature and pressure conditions (Figures 5 and 8). Moreover, it has been shown that [TiChu-PD] is coupled to (and limited by) Ti, whereas there is not apparent limit for [Si]. Therefore, a realistic water solubility law for the upper mantle should capture these features by treating the incorporation of the two defects separately as anticipated by Ingrin et al. (2013). Trivalent defects are not included in the following discussion because of their low concentration (Tables 2 and 3) and their complex relationship with oxygen fugacity (Grant et al., 2007). Nevertheless, hydrated trivalent defects might be relevant during hydrous melting as observed in this (Figure 5 and Table 2) and other experimental studies (Kovács et al., 2012), as well as recorded in mantle xenoliths from some suprasubduction settings (e.g., Soustelle et al., 2010; Tollan et al., 2015).

The occurrence of [Si] might seem at odds given that olivine in our experiments is buffered by orthopyroxene and not by periclase. While low silica activity will favor [Si] through the reaction:

$$\underset{\text{periclase}}{2\,MgO} + \underset{\text{fluid}}{2\,H_2O} = \underset{[Si]}{Mg_2H_4O_4} \quad (1a)$$

and high silica activity imposed by enstatite will favor hydrogen associated to magnesium vacancies [Mg] through the reaction:

$$\underset{\text{enstatite}}{1/2\,Mg_2Si_2O_6} + \underset{\text{fluid}}{H_2O} = \underset{[Mg]}{MgH_2SiO_4}. \quad (1b)$$

[Mg] and [Si] are not mutually incompatible and both are commonly reported in enstatite buffered experiments at 1.5–2.0 GPa; although [Mg] dominates over [Si] (Berry et al., 2005; Lemaire et al., 2004; Matveev et al., 2001). This attests for an internal equilibrium of the two defects in enstatite buffered assemblages of the form:

$$\underset{\text{forsterite}}{2\,Mg_2SiO_4} + \underset{[Mg]}{2\,MgH_2SiO_4} = \underset{\text{enstatite}}{2\,Mg_2Si_2O_6} + \underset{[Si]}{Mg_2H_4O_4}. \quad (1c)$$

It can be concluded that reaction (1c) is displaced toward the right with increasing pressure based on the systematic domination of [Si] over [Mg] in experiments buffered with enstatite at higher pressures ($P \geq 8$ GPa) (e.g., Withers & Hirschmann, 2008). The conclusion of Smyth et al. (2006) that silica activity has a subordinate effect on the type of hydrous defect at extreme pressures ($P = 12$ GPa) is in agreement with this reasoning. Walker et al. (2007) reached the same conclusion based on statistical thermodynamic grounds by showing that high water concentrations in olivine (typical of high-pressure experiments) will favor [Si] over [Mg]. Walker et al. (2007) further suggest that decreasing temperature will have a similar effect than increasing pressure in the proportion of [Si] over [Mg]. This would be in agreement with the observation that [Si] dominates in our low-temperature experiments even at 0.5 GPa (Figure 5). Therefore, at high pressure and low temperature [Si] is determined by the following reaction rather than by (1a):

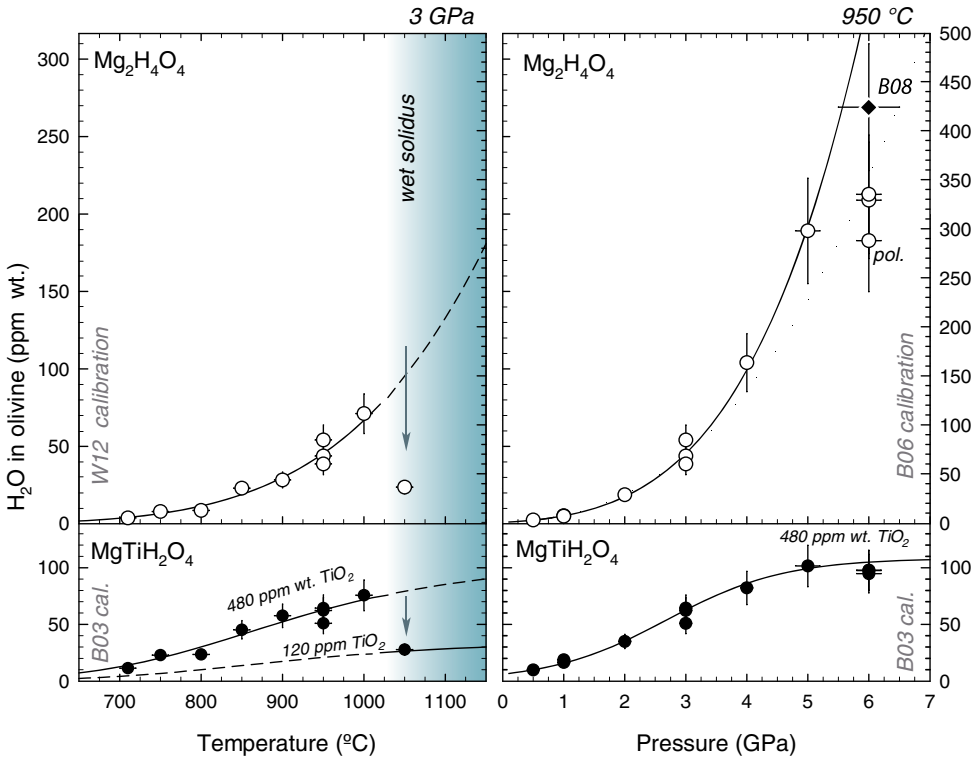


**Figure 8.** Evolution of the water content with temperature and pressure for hydrous defect associated to silicon vacancies [Si] ($Mg_2H_4O_4$) and associated to titano-clinohumite point defects [TiChu-PD] ($MgTiH_2O_4$). Values for [Si] are given using the calibration of (left) Withers et al. (2012) and (right) Bell et al. (2003). Lines are equations (7a) and (7b) for [Si] and equations (8a) and (8b) for [TiChu-PD] assuming a total of 480 and 120 ppm wt $TiO_2$ in olivine. Arrows indicate the effect of wet melting. The fit in Figure 8 (right) does not include the data at 6 GPa. The point labeled with pol. corresponds to the value obtained using polarized IR light, (cf. Table 3). For comparison the datum at 6 GPa (extrapolated from 1000 to 950°C) from Bali et al. (2008) is shown as black diamond (B08). The uncertainty in water content (18%) is estimated based on the uncertainty in the average unpolarized absorbance (10%) and in the calibration factor (15%) added in quadrature.

$$\underset{\text{forsterite}}{2\,Mg_2SiO_4} + \underset{\text{fluid}}{2\,H_2O} = \underset{\text{enstatite}}{Mg_2Si_2O_6} + \underset{[Si]}{Mg_2H_4O_4}. \quad (1d)$$

The incorporation of [TiChu-PD] is controlled by the following reaction where the anhydrous titanium component is either in solid solution in olivine (by tetrahedral substitution of $Ti^{4+}$ for $Si^{4+}$) or in the form of the $Mg_2TiO_4$ spinel (qandilite) (Hermann et al., 2005):

$$\underset{\text{qnd or fo}}{Mg_2TiO_4} + 1/2\,\underset{\text{enstatite}}{Mg_2Si_2O_6} + \underset{\text{fluid}}{H_2O} = \underset{[TiChu\text{-}PD]}{MgTiH_2O_4} + \underset{\text{forsterite}}{Mg_2SiO_4}. \quad (2)$$

Note that other equations might be written by considering Ti-bearing endmembers in pyroxenes and garnet. Interestingly, reactions (1d) and (2) can be combined given an expression independent of the water activity (fluid absent reaction) which controls the ratio of [TiChu-PD] over [Si] defects:

$$\underset{\text{forsterite}}{2\,Mg_2SiO_4} + \underset{[TiChu\text{-}PD]}{2\,MgTiH_2O_4} = \underset{\text{enstatite}}{Mg_2Si_2O_6} + \underset{\text{qnd/fo}}{Mg_2TiO_4} + \underset{[Si]}{Mg_2H_4O_4}. \quad (3)$$

For simplicity we will assume that the relations in the $TiO_2$-MgO-$SiO_2$-$H_2O$ system discussed above apply to our natural composition and therefore equilibria are governed only by the activities of the hydrous components in olivine (e.g., the effect of ferromagnesium exchange will be neglected) and the activity of $H_2O$ in the fluid, which is essentially pure at subsolidus conditions. Under these conditions and assuming that hydrogen is fully ordered in the tetrahedral site (molecular mixing model), the dependence of [Si] concentration (expressed as hydrogen in atoms per formula unit, $H_{[Si]}$(apfu), dimensionless) on pressure and temperature for a pure $H_2O$ fluid is given by

$$RT\ln X^{ol}_{Mg_2H_4O_4} = RT\ln H_{[Si]}(apfu)/4 = -\Delta_r G^{\circ}_{(T,1\ bar)}(1d) - RT\ln\gamma^{ol,\infty}_{Mg_2H_4O_4} - \int_1^P \Delta_r V_{(T,s)}(1d)dP + 2RT\ln f^*_{H_2O}$$
$$= -\Delta_r G^*_{(T,1\ bar)}(1d) - \int_1^P \Delta_r V_{(T,s)}(1d)dP + 2RT\ln f^*_{H_2O}, \quad (4)$$

where $\Delta_r G^*_{(T,1\ bar)}$ in J mol$^{-1}$ refers to a standard state of infinite dilution and $f^*_{H_2O}$ is the dimensionless water fugacity, that is, $f_{H_2O}$ in bars normalized to $f^{\circ}_{H_2O}$ (1 bar). Although traditionally water concentrations in similar expressions in the literature are reported as ppm or atomic ratio as H/10$^6$Si (e.g., Bali et al., 2008), we rather prefer mole fractions to maintain thermodynamically consistent units in the above expression (a description to transform ppm values to atoms per formula and mole fractions is detailed and an the excel file in the supporting information). Similarly, for [TiChu-PD],

$$RT\ln\frac{X^{ol}_{MgTiH_2O_4}}{X^{ol,qd}_{Mg_2TiO_4}} = RT\ln\frac{H_{[TiChu-PD]}(apfu)/2}{Ti^{4+}_{total}(apfu) - H_{[TiCh-PD]}(apfu)/2} = -\Delta_r G^*_{(T,1\ bar)}(2) - \int_1^P \Delta_r V_{(T,s)}(2)dP + RT\ln f^*_{H_2O,} \quad (5)$$

where $Ti^{4+}_{total}$[atoms per formula unit] refers to the sum of $Ti^{4+}$ in hydrous and anhydrous defects, which is related to the $TiO_2$ in wt % in the olivine structural formula unit as

$$Ti^{4+}_{total}[apfu] = {}^{14,073\cdot TiO_2[wt\%]}\Big/_{(1,979\cdot TiO_2[wt\%])+798,800.} \quad (6)$$

Most probably, this value varies in the investigated pressure and temperature range (Figure 6), but given the lack of experimental data constraining this variation, it will be assumed constant in the following and equal to the maximum value reported in the literature (480 wt ppm $TiO_2$). Indeed, anhydrous Ti solubility in olivine at temperature between 800 and 1000°C is expected to range from 2 to 20 ppm wt (Hermann et al., 2005) contributing little to $Ti^{4+}_{total}$[apfu]. The 1:2 slope observed between Ti and H (Figure 7) in molar units further supports that most of the Ti is associated to hydrous defects and therefore octahedrally coordinated at subsolidus conditions. The same correlation has been recently obtained independently by Tollan et al. (2017).

A multiple regression analysis by least squares of the all data set (excluding data at supersolidus conditions and at 6 GPa, see below) results in (Figure 8, calibration from Bell et al., 2003):

$$RT\ln X^{ol}_{Mg_2H_4O_4}\ [J\ mol^{-1}] = -5.8\cdot10^5 + 14\cdot T[K] + 4.43\cdot10^4\cdot\ln\left((2.1 + P[GPa])\cdot10^4\right) \quad (7a)$$

relative to reaction (1d). The following expression converts mole fractions of $MgH_4O_4$ to ppm wt $H_2O$ (see Text S1 and the accompanying document in the supporting information):

$$C^{[Si]}_{H_2O}\ [ppm\ wt\ H_2O] = \frac{360,400\cdot4\cdot X^{ol}_{Mg_2H_4O_4}}{56,292 - 2,405\cdot4\cdot X^{ol}_{Mg_2H_4O_4}}\cdot10,000. \quad (7b)$$

A factor of 0.119/0.188 (0.633) should be applied to transform equation (7b) into ppm wt $H_2O$ using the calibration of Withers et al. (2012). Although the location of the wet solidus is debated at $P > 5$ GPa, extrapolation of equation (7a) to higher pressure allows a tentative comparison with previous experimental studies interpreted to be also subsolidus. The datum of Bali et al. (2008) at 6 GPa (417 ± 60 ppm wt $H_2O$ when extrapolated to 950°C from 1000°C, 548 ppm) is in agreement with the prediction of the fit (542 ± 80 ppm, Figure 8) and suggests that the data from the present study at 6 GPa and 950°C might underestimate the actual water content by 25% likely due to pressure instability during long run duration of the ultrahigh pressure piston cylinder. The datum at 6 GPa and 1100°C (1,189 ± 180 ppm) from Bali et al. (2008) nicely compares with the predicted value by equations (7a) and (7b) (1,274 ± 190 ppm). This is further corroborated by the data of Mosenfelder et al. (2006) at 8 GPa 1100°C (3,007–3,035 ppm versus, 3,000 ± 450 ppm from equations (7a) and (7b)). At higher pressure, however, equations (7a) and (7b) predict water contents that are significantly higher than those observed experimentally. For instance, at 12 GPa and 1100°C, Mosenfelder et al. (2006) found 6,399 ppm and Smyth et al. (2006) found 5,770 ppm, whereas the prediction of equations (7a) and (7b) is 10,964 ppm ± 1,600 ppm. Because equations (7a) and (7b) have been derived from subsolidus conditions where the fluid can be considered nearly pure $H_2O$, the observed discrepancy with the experimental data at $P \geq 10$ GPa is indicative of an important solubility of silicates in the fluid that reduces the water fugacity when approaching the second critical endpoint in the ultramafic system (approximately 10–12 GPa and 1100–1150°C, e.g., Stalder & Ulmer, 2001; Hermann et al., 2006). Indeed, a lowering of the

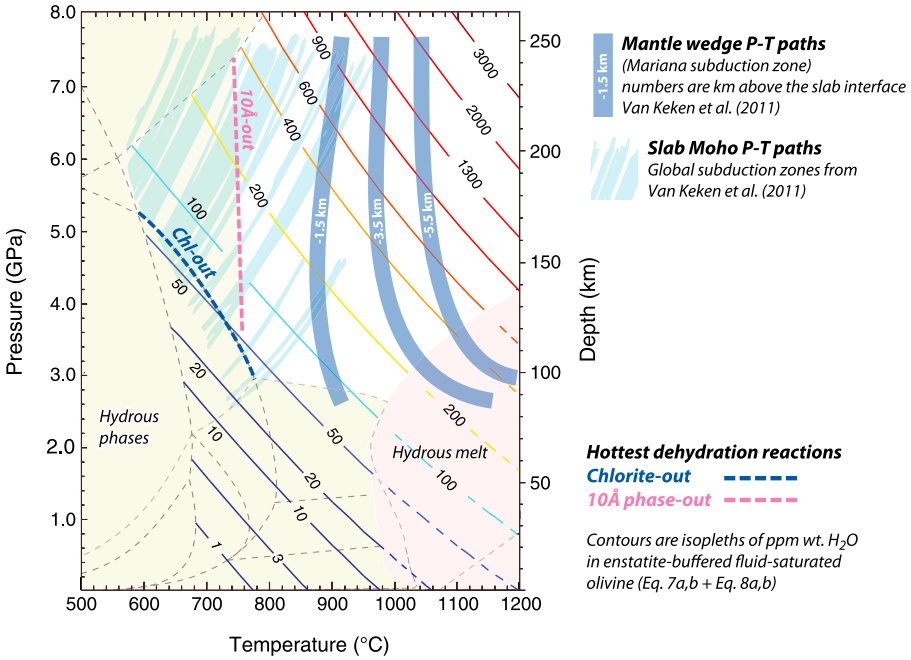


**Figure 9.** Contours of the total water content in olivine in ppm wt $H_2O$ ([TiChu-PD] equations (7a) and (7b) using 480 ppm $TiO_2$ + [Si] equations (8a) and (8b)) as a function of pressure and temperature relevant for subduction zone settings. The stability of hydrous phases (antigorite, talc, chlorite, amphibole, phase-A, and 10A-phase) is indicated by the green field. Water content in the hydrous melt region (red field from Green, 1973, cf. Figure 1) corresponds to water saturation only (dashed contour lines). Superimposed are the P-T trajectories at Moho depths of global subduction zones from the numerical models of van Keken et al. (2011); these trajectories cut the chlorite-out and 10 Å phase-out (Fumagalli & Poli, 2005) defining the olivine water content at fluid saturation conditions (maximum storage capacity of the subducting slab). Thick bands are numerically computed P-T trajectories of the mantle wedge at different distances from the slab surface.

water activity from 1 to 0.7 will lead to a 50% decrease in the water incorporation in [Si] defects in olivine (Tollan et al., 2017).

Reaction (2) controlling the incorporation of [TiChu-PD] can be fitted by following expression, which is linear with pressure (calibration from Bell et al., 2003):

$$RT\ln\frac{X^{ol}_{MgTiH_2O_4}}{X^{ol,qd}_{Mg_2TiO_4}}\left[\text{J mol}^{-1}\right] = -1.24{\cdot}10^5 + 78{\cdot}T[\text{K}] + 1.06{\cdot}10^4{\cdot}P[\text{GPa}], \tag{8a}$$

where $X^{ol}_{MgTiH_2O_4} = Ti^{4+}_{total}[\text{apfu}]\cdot\exp(\text{equation 8a})/(\exp(\text{equation 8a}) + 1)$. The following expression converts mole fractions of $MgTiH_2O_4$ to ppm wt $H_2O$ (an excel file for computing equations (7a), (7b), (8a), and (8b) as a function of total $Ti^{4+}$ in olivine is provided in the supporting information):

$$C^{[\text{TiChu}-\text{PD}]}_{H_2O}\ [\text{ppm wt } H_2O] = \frac{180,200{\cdot}2{\cdot}X^{ol}_{Mg_2Ti_2H_2O_4}}{28,146 - 249{\cdot}2{\cdot}X^{ol}_{Mg_2Ti_2H_2O_4}}{\cdot}10,000. \tag{8b}$$

The amount [TiChu-PD] will be eventually controlled by the availability of titanium in the bulk peridotite (e.g., mantle fertility and/or metasomatism) and its solubility in olivine ( $Ti^{4+}_{total}[\text{apfu}]$). An equivalent expression for reaction (3) can be found by combining (7a) and (7b), and (8a) and (8b) giving the ratio of [Si] over [TiChu-PD] with pressure and temperature. This ratio is mostly pressure dependent, which is in agreement with the dominant occurrence of [Si] over [TiChu-PD] commonly observed in kimberlitic olivine from the deepest part of the cratonic mantle (Doucet et al., 2014; Matveev & Stachel, 2007). It is worth to mention that the total water content obtained by summing equations (7a), (7b), (8a), and (8b) (119–185 ppm wt $H_2O$) nicely fits the subsolidus data in the $TiO_2$-MgO-$SiO_2$-$H_2O$ synthetic system (86–168 ppm wt $H_2O$) recently investigated independently by Tollan et al. (2017) at 3 GPa and 1050°C ($R^2$ = 0.90, based on five experiments at $H_2O$ saturated conditions where $TiO_2$ contents range from 150 to 550 ppm wt).

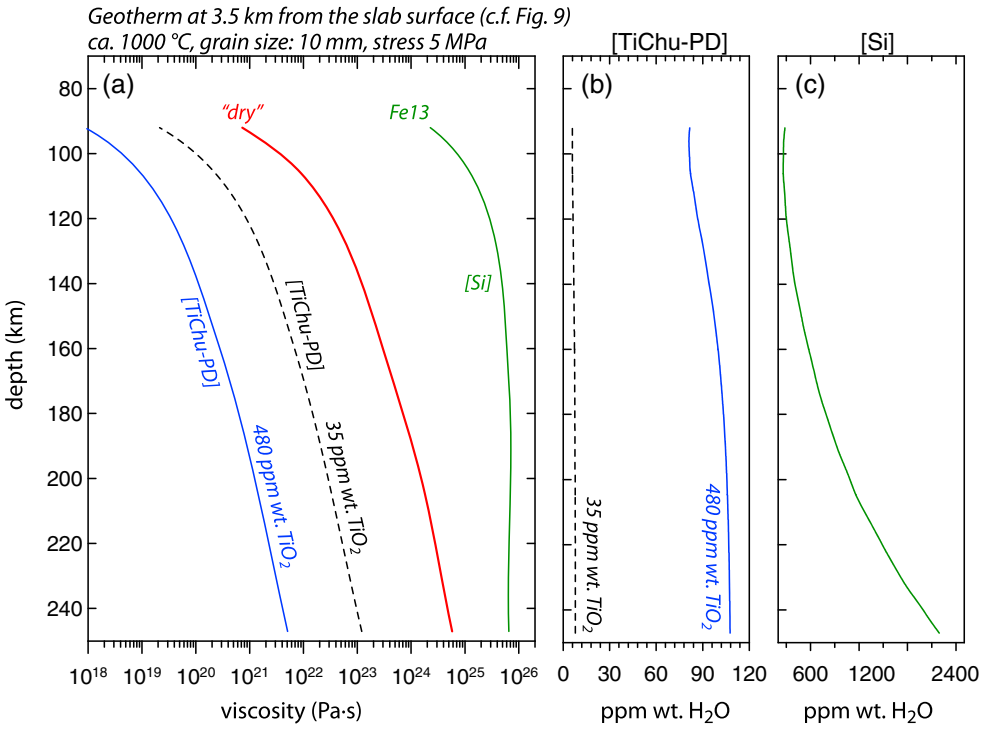


**Figure 10.** (a) Example of maximum rheological effect of hydrous defects associated to Si vacancies either associated to Ti [TiChu-PD] (using the expression from Faul et al., 2016 and equations (8a) and (8b) or pure Si vacancies [Si] (Fei et al., 2013, and equations (7a) and (7b), curve labeled as Fe13) along a geotherm in the mantle wedge located at 3.5 km from the slab surface (cf. Figure 9). (b) Evolution of maximum [TiChu-PD] for 480 (continuous line) and 35 ppm wt $TiO_2$ in olivine (dashed line). (c) Evolution of [Si] with pressure.

## 5. Implications

### 5.1. Deep Water Recycling Subduction Zones

The new subsolidus solubility law presented above enables to compute the maximum water content in olivine for the cold- and high-pressure conditions of the subducting slab and to estimate the potential of the mantle wedge coupled to the subducted slab as water carrier into the deep Earth. In the first case, the maximum water content in olivine is constrained at the conditions where the hottest dehydration reactions intersect the pressure-temperature (P-T) trajectories of the hydrated subducting slab releasing aqueous fluid. Chlorite dehydration is roughly parallel to the isopleth of 50 ± 20 ppm wt $H_2O$ (dashed blue line in Figure 9); this implies a bulk water content retained in the slab mantle of approximately 90 ± 20 ppm wt $H_2O$ (assuming a model harzburgite from Schmidt & Poli, 1998; 200 and 6 ppm wt $H_2O$ in orthopyroxene and garnet, respectively, and a partition coefficient $Kd^{cpx/opx}$ of 2.1, Demouchy & Bolfan-Casanova, 2016, Demouchy et al., 2017). This value is roughly independent on the specific P-T trajectory followed by the slab (Figure 9) and is significantly lower than previous estimates (400 ppm wt $H_2O$, Arcay et al., 2005). The potential for higher storage capacity of the slab is significantly increased if the 10 Å phase is the last and hottest dehydration reaction to be intersected (Fumagalli & Poli, 2005). In this case the water storage capacity in the slab mantle is highly dependent on the P-T trajectory of the slab ranging from 50 to 400 ppm wt in olivine, which translates into a bulk storage capacity of 90–340 ppm wt $H_2O$ (using the same assumption as above).

Previous workers have stressed the importance of water incorporation into NAMs in the mantle wedge as an effective way to transport water into the deep Earth's interior (Hebert & Montési, 2013; Horiuchi & Iwamori, 2016; Iwamori, 2007). Hydrous defects are dominated by Si vacancies under the relevant conditions for the mantle wedge ($T > 900$°C and $P > 3$ GPa, Figure 8). Maximum olivine water storage capacity along P-T trajectories at different distances from the slab interface of the Mariana subduction zone modeled by van Keken et al. (2011) are presented in Figure 9. At 1.5 km from the slab surface the storage capacity ranges from 100 to 900 ppm, whereas at 5.5 km, which follows an isotherm of approximately 1100°C, it ranges from 400 to 2,000 ppm. It is unlikely that higher water contents at higher distances from the slab surface can be

achieved given the important effect that melting has on reducing the water solubility in olivine (Figure 8). Moreover, the Mariana subduction zone, which is one of the coldest slabs worldwide, might represent an upper bound of maximum water transfer to the mantle wedge (a deeper dehydration in the slab results in higher water solubility on top of the slab). Although the position of the hydrous melting and the second critical end point are largely unconstrained at these conditions, the maximum storage capacity in olivine from the upper mantle wedge probably would not exceed 3,000 ppm (that translates into a maximum of 2,240 ppm bulk $H_2O$, assuming 400 ppm wt $H_2O$ in opx and a $Kd^{cpx/opx}$ of 2.1) that corresponds to an isotherm of approximately 1150°C (cf. wet solidi from Green, 1973; Green et al., 2010; Kushiro et al., 1968; Kawamoto & Holloway, 1997, Figures 1 and 9). This contrasts with previous estimates, not only in the value of the storage capacity (400 ppm in Arcay et al., 2005; 1,100–4,200 ppm in Iwamori, 2007; 3,000–4,000 ppm in Horiuchi & Iwamori, 2016) but more importantly in the distance from the slab surface ($<$5 km) to which the NAMs from the mantle wedge can be hydrated (20–40 km in Iwamori, 2007; Horiuchi & Iwamori, 2016, and 20–30 km in Arcay et al., 2005).

### 5.2. Impact on Rheology

Recent experimental studies have suggested that pure hydrated Si vacancies [Si] have a minor effect on Si diffusion and therefore on deformation in the diffusion creep regime (at 8 GPa, Fei et al., 2013), whereas hydrous defects associated to Ti strongly enhance deformation in the dislocation and diffusion creep regime (at 0.3 GPa, Faul et al., 2016, and references therein). Although this contrasting behavior is not yet fully understood, the dissimilar rheological effect between the two of hydrous defects involving Si vacancies could be explained in terms of different intrinsic diffusivities being significantly faster for [TiChu-PD] and with lower activation energy than for [Si] (Padrón-Navarta et al., 2014). Most importantly, the present study allows evaluating individually the rheological effect (if any) of the two types of defects. This is illustrated using as example the mantle wedge located at 3.5 km from the slab surface (Figure 10), where subsolidus and fluid saturation conditions (required to apply equations (7a), (7b), (8a), and (8b)) are most likely to be met (cf. Figure 9). Figure 10a shows the evolution of viscosity with depth using the expression given by Faul et al. (2016, their equation (1) and their Table 2, dislocation and diffusion creep regime) and Fei et al. (2012, exclusively diffusion creep through the effect of [Si] on Si self-diffusion), where the water concentration in olivine (either [TiChu-PD] and [Si] respectively, Figures 10b and 10c) is here computed explicitly as a function of pressure and temperature and not treated as a constant as in previous works. A constant value of stress of 5 MPa is assumed for illustrative purposes although stresses along the geotherm at 3.5 km from the slab are most probably in the range of 3 to 10 MPa in this region (Kneller et al., 2005). The saturation of [TiChu-PD] for a bulk $TiO_2$ of 480 ppm wt (approximately 100 ppm) is reached at relatively shallow conditions (100–150 km) resulting in a viscosity drop of 3 orders of magnitude compared to the dry rheology (Figure 10a). The rheological effect is still significant (1.5 orders of magnitude weaker) even for the case of a depleted mantle wedge having only 35 ppm wt of $TiO_2$ (dashed line in Figures 10a and 10b). Water solubility related to [Si] defects along this particular geotherm is significantly higher (300–2,000 ppm, Figure 10c) than those of [TiChu-PD]. However, such high contents do not lower mantle wedge viscosity (Figure 10) using the expression given by Fei et al. (2013). If true, this would imply that even comparatively small amounts of [TiChu-PD] (as low as 8 ppm wt $H_2O$ equivalent to 35 ppm wt $TiO_2$) overwhelm the rheological effect of [Si]. As a consequence, water storage capacity and therefore the level of $H_2O$ needed to reach fluid saturation (which will activate other deformation mechanisms, e.g., Tommasi et al., 2017) is controlled by [Si] defects, whereas minor variation of Ti contents might modify mantle rheology. Such complex dichotomy can now be explored by using individual solubility laws as proposed here.

**Acknowledgments**
The authors thank the Associate Editor, A. Peslier, and one anonymous reviewer for constructive comments. The research leading to these results has been funded by HISLa-DR, an EU FP7 Marie Curie Action under grant agreement PIOF-GA-2010-273017 and ANR-16-TERC-0013-01 TREMPLIN ERC 2016. We thank Dean Scott and Dave Clark for their technical support in the running of the high-pressure experiments at the RSES (ANU) and B. Boyer (Microsonde Sud, France) for his technical assistance in the EPMA analyses. I. Kovács and collaborators are thanked for providing some of the digital IR spectra shown in Figure 4 through the PULI database. S. Demouchy, A. Tommasi, C. Thoraval, and D. Arcay are acknowledged for discussion about the rheological effect of hydrous defects on olivine. M. Cotte is also thanked for allowing access to the synchrotron facilities at ESRF for the FTIR measurements. All data presented here can be obtained by e-mailing the corresponding author.

## References

Aradi, L. E., Hidas, K., Kovács, I. J., Tommasi, A., Klébesz, R., Garrido, C. J., & Szabó, C. (2017). Fluid-enhanced annealing in the subcontinental lithospheric mantle beneath the westernmost margin of the Carpathian-Pannonian extensional basin system. *Tectonics*, *36*. https://doi.org/10.1002/2017TC004702

Arcay, D., Tric, E., & Doin, M. P. (2005). Numerical simulations of subduction zones: Effect of slab dehydration on the mantle wedge dynamics. *Physics of the Earth and Planetary Interiors*, *149*(1-2), 133–153. https://doi.org/10.1016/j.pepi.2004.08.020

Ardia, P., Hirschmann, M. M., Withers, A. C., & Tenner, T. J. (2012). $H_2O$ storage capacity of olivine at 5–8 GPa and consequences for dehydration partial melting of the upper mantle. *Earth and Planetary Science Letters*, *345–348*, 104–116.

Bali, E., Bolfan-Casanova, N., & Koga, K. T. (2008). Pressure and temperature dependence of H solubility in forsterite: An implication to water activity in the Earth interior. *Earth and Planetary Science Letters*, *268*(3-4), 354–363. https://doi.org/10.1016/j.epsl.2008.01.035

Bell, D. R., Ihinger, P. D., & Rossman, G. R. (1995). Quantitative analysis of trace OH in garnet and pyroxenes. *American Mineralogist*, *80*(5-6), 465–474. https://doi.org/10.2138/am-1995-5-607

Bell, D.R., Rossman, G.R., Maldener, J., Endisch, D., and Rauch, F. (2003). Hydroxide in olivine: A quantitative determination of the absolute amount and calibration of the IR spectrum. *Journal of Geophysical Research 108*(B2), 2105. https://doi.org/10.1029/2001JB000679

Berry, A. J., Hermann, J., O'Neill, H. S. C., & Foran, G. J. (2005). Fingerprinting the water site in mantle olivine. *Geology*, *33*(11), 869–872. https://doi.org/10.1130/G21759.1

Berry, A. J., Walker, A. M., Hermann, J., O'Neill, H. S., Foran, G. J., & Gale, J. D. (2007). Titanium substitution mechanisms in forsterite. *Chemical Geology*, *242*(1-2), 176–186. https://doi.org/10.1016/j.chemgeo.2007.03.010

Blanchard, M., Ingrin, J., Balan, E., Kovács, I., & Withers, A. C. (2017). Effect of iron and trivalent cations on OH defects in olivine. *American Mineralogist*, *102*(2), 302–311.

Connolly, J. A. D. (2009). The geodynamic equation of state: What and how. *Geochemistry, Geophysics, Geosystems*, *10*, Q10014. https://doi.org/10.1029/2009GC002540

Costa, F., & Chakraborty, S. (2008). The effect of water on Si and O diffusion rates in olivine and implications for transport properties and processes in the upper mantle. *Physics of the Earth and Planetary Interiors*, *166*(1-2), 11–29. https://doi.org/10.1016/j.pepi.2007.10.006

Demouchy, S., & Bolfan-Casanova, N. (2016). Distribution and transport of hydrogen in the lithospheric mantle: A review. *Lithos*, *240–243*, 402–425.

Demouchy, S., & Mackwell, S. (2006). Mechanisms of hydrogen incorporation and diffusion in iron-bearing olivine. *Physics and Chemistry of Minerals*, *33*(5), 347–355. https://doi.org/10.1007/s00269-006-0081-2

Demouchy, S., Shcheka, S., Denis, C. M. M., & Thoraval, C. (2017). Subsolidus hydrogen partitioning between nominally anhydrous minerals in garnet-bearing peridotite. *American Mineralogist*, *102*(9), 1822–1831. https://doi.org/10.2138/am-2017-6089

Demouchy, S., Tommasi, A., Barou, F., Mainprice, D., & Cordier, P. (2012). Deformation of olivine in torsion under hydrous conditions. *Physics of the Earth and Planetary Interiors*, *202–203*, 56–70.

Doucet, L. S., Peslier, A. H., Ionov, D. A., Brandon, A. D., Golovin, A. V., Goncharov, A. G., & Ashchepkov, I. V. (2014). High water contents in the Siberian cratonic mantle linked to metasomatism: An FTIR study of Udachnaya peridotite xenoliths. *Geochimica et Cosmochimica Acta*, *137*, 159–187. https://doi.org/10.1016/j.gca.2014.04.011

Faul, U. H., Cline, C. J. II, David, E. C., Berry, A. J., & Jackson, I. (2016). Titanium-hydroxyl defect-controlled rheology of the Earth's upper mantle. *Earth and Planetary Science Letters*, *452*, 227–237. https://doi.org/10.1016/j.epsl.2016.07.016

Fei, H., Wiedenbeck, M., Yamazaki, D., & Katsura, T. (2013). Small effect of water on upper-mantle rheology based on silicon self-diffusion coefficients. *Nature*, *498*(7453), 213–215. https://doi.org/10.1038/nature12193

Férot, A., & Bolfan-Casanova, N. (2012). Water storage capacity in olivine and pyroxene to 14 GPa: Implications for the water content of the Earth's upper mantle and nature of seismic discontinuities. *Earth and Planetary Science Letters*, *349-350*, 218–230. https://doi.org/10.1016/j.epsl.2012.06.022

Ferriss, E., Plank, T., & Walker, D. (2016). Site-specific hydrogen diffusion rates during clinopyroxene dehydration. *Contributions to Mineralogy and Petrology*, *171*, 1–24.

Fumagalli, P., & Poli, S. (2005). Experimentally determined phase relations in hydrous peridotites to 6.5 GPa and their consequences on the dynamics of subduction zones. *Journal of Petrology*, *46*, 555–578.

Gaetani, G., O'Leary, J., Koga, K., Hauri, E., Rose-Koga, E., & Monteleone, B. (2014). Hydration of mantle olivine under variable water and oxygen fugacity conditions. *Contributions to Mineralogy and Petrology*, *167*, 1–14.

Girard, J., Chen, J., Raterron, P., & Holyoke, C. W. (2013). Hydrolytic weakening of olivine at mantle pressure: Evidence of [100](010) slip system softening from single-crystal deformation experiments. *Physics of the Earth and Planetary Interiors*, *216*, 12–20. https://doi.org/10.1016/j.pepi.2012.10.009

Grant, K. J., Brooker, R. A., Kohn, S. C., & Wood, B. J. (2007). The effect of oxygen fugacity on hydroxyl concentrations and speciation in olivine: Implications for water solubility in the upper mantle. *Earth and Planetary Science Letters*, *261*(1-2), 217–229. https://doi.org/10.1016/j.epsl.2007.06.024

Green, D. H. (1973). Experimental melting studies on a model upper mantle composition at high pressure under water-saturated and water-undersaturated conditions. *Earth and Planetary Science Letters*, *19*(1), 37–53. https://doi.org/10.1016/0012-821X(73)90176-3

Green, D. H., Hibberson, W. O., Kovács, I., & Rosenthal, A. (2010). Water and its influence on the lithosphere-asthenosphere boundary. *Nature*, *467*(7314), 448–451. https://doi.org/10.1038/nature09369

Grove, T. L., Chatterjee, N., Parman, S. W., & Médard, E. (2006). The influence of $H_2O$ on mantle wedge melting. *Earth and Planetary Science Letters*, *249*(1-2), 74–89. https://doi.org/10.1016/j.epsl.2006.06.043

Hacker, B. R. (2008). $H_2O$ subduction beyond arcs. *Geochemistry, Geophysics, Geosystems*, *9*, Q03001. https://doi.org/10.1029/2007GC001707

Hacker, B. R., Sharp, T., Zhang, R. Y., Liou, J. G., & Hervig, R. L. (1997). Determining the origin of ultrahigh-pressure lherzolites. *Science*, *278*(5338), 702–704.

Hebert, L. B., Antoshechkina, P., Asimow, P., & Gurnis, M. (2009). Emergence of a low-viscosity channel in subduction zones through the coupling of mantle flow and thermodynamics. *Earth and Planetary Science Letters*, *278*(3-4), 243–256. https://doi.org/10.1016/j.epsl.2008.12.013

Hebert, L. B., & Montési, L. G. J. (2013). Hydration adjacent to a deeply subducting slab: The roles of nominally anhydrous minerals and migrating fluids. *Journal of Geophysical Research: Solid Earth*, *118*(11), 5753–5770. https://doi.org/10.1002/2013JB010497

Hermann, J., O'Neill, H. S. C., & Berry, A. J. (2005). Titanium solubility in olivine in the system $TiO_2$-MgO-$SiO_2$: No evidence for an ultra-deep origin of Ti-bearing olivine. *Contributions to Mineralogy and Petrology*, *148*(6), 746–760. https://doi.org/10.1007/s00410-004-0637-4

Hermann, J., Spandler, C., Hack, A., & Korsakov, A. V. (2006). Aqueous fluids and hydrous melts in high-pressure and ultra-high pressure rocks: Implications for element transfer in subduction zones. *Lithos*, *92*(3-4), 399–417. https://doi.org/10.1016/j.lithos.2006.03.055

Hervig, R. L., Smith, J. V., & Dawson, J. B. (1986). Lherzolite xenoliths in kimberlites and basalts: Petrogenetic and crystallochemical significance of some minor and trace elements in olivine, pyroxenes, garnet and spinel. *Earth and Environmental Science Transactions of the Royal Society of Edinburgh*, *77*(03), 181–201.

Hirschmann, M. M. (2006). Water, melting, and the deep Earth $H_2O$ cycle. *Annual Review of Earth and Planetary Sciences*, *34*(1), 629–653. https://doi.org/10.1146/annurev.earth.34.031405.125211

Horiuchi, S.-S., & Iwamori, H. (2016). A consistent model for fluid distribution, viscosity distribution, and flow-thermal structure in subduction zone. *Journal of Geophysical Research: Solid Earth*, *121*(5), 3238–3260. https://doi.org/10.1002/2015JB012384

Ingrin, J., Liu, J., Depecker, C., Kohn, S. C., Balan, E., & Grant, K. J. (2013). Low-temperature evolution of OH bands in synthetic forsterite, implication for the nature of H defects at high pressure. *Physics and Chemistry of Minerals*, *40*(6), 499–510. https://doi.org/10.1007/s00269-013-0587-3

Iwamori, H. (2007). Transportation of $H_2O$ beneath the Japan arcs and its implications for global water circulation. *Chemical Geology*, *239*(3-4), 182–198. https://doi.org/10.1016/j.chemgeo.2006.08.011

Jollands, M. C., Padrón-Navarta, J. A., Hermann, J., & O'Neill, H. S. C. (2016). Hydrogen diffusion in Ti-doped forsterite and the preservation of metastable point defects. *American Mineralogist*, *101*(7), 1571–1583. https://doi.org/10.2138/am-2016-55681571

Kawamoto, T., & Holloway, J. R. (1997). Melting temperature and partial melt chemistry of $H_2O$-saturated mantle peridotite to 11 gigapascals. *Science*, *276*(5310), 240–243. https://doi.org/10.1126/science.276.5310.240

Kneller, E. A., van Keken, P. E., Karato, S., & Park, J. (2005). B-type olivine fabric in the mantle wedge: Insights from high-resolution non-Newtonian subduction zone models. *Earth and Planetary Science Letters*, *237*(3-4), 781–797. https://doi.org/10.1016/j.epsl.2005.06.049

Kohlstedt, D. L., Keppler, H., & Rubie, D. C. (1996). Solubility of water in the $\alpha$, $\beta$ and $\gamma$ phases of $(Mg,Fe)_2SiO_4$. *Contributions to Mineralogy and Petrology*, *123*(4), 345–357. https://doi.org/10.1007/s004100050161

Kovács, I., Green, D. H., Rosenthal, A., Hermann, J., O'Neill, H. S. C., Hibberson, W. O., & Udvardi, B. (2012). An experimental study of water in nominally anhydrous minerals in the upper mantle near the water-saturated solidus. *Journal of Petrology*, *53*(10), 2067–2093. https://doi.org/10.1093/petrology/egs044

Kovács, I., Hermann, J., O'Neill, H. S. C., Gerald, J. F., Sambridge, M., & Horvath, G. (2008). Quantitative absorbance spectroscopy with unpolarized light: Part II. Experimental evaluation and development of a protocol for quantitative analysis of mineral IR spectra. *American Mineralogist*, *93*(5-6), 765–778. https://doi.org/10.2138/am.2008.2656

Kushiro, I., Syono, Y., & Akimoto, S.-I. (1968). Melting of a peridotite nodule at high pressures and high water pressures. *Journal of Geophysical Research*, *73*(18), 6023–6029. https://doi.org/10.1029/JB073i018p06023

Lemaire, C., Kohn, S. C., & Brooker, R. A. (2004). The effect of silica activity on the incorporation mechanisms of water in synthetic forsterite: A polarised infrared spectroscopic study. *Contributions to Mineralogy and Petrology*, *147*, 48–57.

López Sánchez-Vizcaíno, V., Trommsdorff, V., Gómez-Pugnaire, M. T., Garrido, C. J., Müntener, O., & Connolly, J. A. D. (2005). Petrology of titanian clinohumite and olivine at the high-pressure breakdown of antigorite serpentinite to chlorite harzburgite (Almirez Massif, S. Spain). *Contributions to Mineralogy and Petrology*, *149*(6), 627–646. https://doi.org/10.1007/s00410-005-0678-3

Mackwell, S. J., & Kohlstedt, D. L. (1990). Diffusion of hydrogen in olivine: Implications for water in the mantle. *Journal of Geophysical Research*, *95*(B4), 5079–5088. https://doi.org/10.1029/JB095iB04p05079

Mackwell, S. J., Kohlstedt, D. L., & Paterson, M. S. (1985). The role of water in the deformation of olivine single crystals. *Journal of Geophysical Research*, *90*(B13), 11,319–11,333. https://doi.org/10.1029/JB090iB13p11319

Marchesi, C., Garrido, C. J., Padrón-Navarta, J. A., López Sánchez-Vizcaíno, V., & Gómez-Pugnaire, M. T. (2013). Element mobility from seafloor serpentinization to high-pressure dehydration of antigorite in subducted serpentinite: Insights from the Cerro del Almirez ultramafic massif (southern Spain). *Lithos*, *15*, 128–142.

Matveev, S., O'Neill, H. S. C., Ballhaus, C., Taylor, W. R., & Green, D. H. (2001). Effect of silica activity on OH- IR spectra of olivine: Implications for low-$aSiO_2$ mantle Metasomatism. *Journal of Petrology*, *42*(4), 721–729. https://doi.org/10.1093/petrology/42.4.721

Matveev, S., & Stachel, T. (2007). FTIR spectroscopy of OH in olivine: A new tool in kimberlite exploration. *Geochimica et Cosmochimica Acta*, *71*(22), 5528–5543. https://doi.org/10.1016/j.gca.2007.08.016

Mei, S., & Kohlstedt, D. L. (2000). Influence of water on plastic deformation of olivine aggregates: 1. Diffusion creep regime. *Journal of Geophysical Research: Solid Earth*, *105*(B9), 21,457–21,469. https://doi.org/10.1029/2000JB900179

Mosenfelder, J. L., Deligne, N. I., Asimow, P. D., & Rossman, G. R. (2006). Hydrogen incorporation in olivine from 2–12 GPa. *American Mineralogist*, *91*(2-3), 285–294. https://doi.org/10.2138/am.2006.1943

Padrón-Navarta, J. A., Hermann, J., & O'Neill, H. S. C. (2014). Site-specific hydrogen diffusion rates in forsterite. *Earth and Planetary Science Letters*, *392*, 100–112. https://doi.org/10.1016/j.epsl.2014.01.055

Padrón-Navarta, J. A., López Sánchez-Vizcaíno, V., Garrido, C. J., & Gómez-Pugnaire, M. T. (2011). Metamorphic record of high-pressure dehydration of antigorite serpentinite to chlorite harzburgite in a subduction setting (Cerro del Almirez, Nevado–Filábride Complex, southern Spain). *Journal of Petrology*, *52*(10), 2047–2078. https://doi.org/10.1093/petrology/egr039

Pearson, D. G., Brenker, F. E., Nestola, F., McNeill, J., Nasdala, L., Hutchison, M. T., … Vincze, L. (2014). Hydrous mantle transition zone indicated by ringwoodite included within diamond. *Nature*, *507*(7491), 221–224. https://doi.org/10.1038/nature13080

Peslier, A. H., Schönbächler, M., Busemann, H., & Karato, S.-I. (2017). Water in the Earth's interior: Distribution and origin. *Space Science Reviews*, *212*(1-2), 743–810. https://doi.org/10.1007/s11214-017-0387-z

Ringwood, A. E., & Major, A. (1967). Some high-pressure transformations of geophysical significance. *Earth and Planetary Science Letters*, *2*(2), 106–110. https://doi.org/10.1016/0012-821X(67)90109-4

Risold, A. C., Trommsdorff, V., & Grobety, B. (2003). Morphology of oriented ilmenite inclusions in olivine from garnet peridotites (central Alps, Switzerland). *European Journal of Mineralogy*, *15*(2), 289–294. https://doi.org/10.1127/0935-1221/2003/0015-0289

Scambelluri, M., Pettke, T., Rampone, E., Godard, M., & Reusser, E. (2014). Petrology and trace element budgets of high-pressure peridotites indicate Subduction dehydration of serpentinized mantle (Cima di Gagnone, central Alps, Switzerland). *Journal of Petrology*, *55*(3), 459–498. https://doi.org/10.1093/petrology/egt068

Schmädicke, E., Gose, J., Witt-Eickschen, G., & Brätz, H. (2013). Olivine from spinel peridotite xenoliths: Hydroxyl incorporation and mineral composition. *American Mineralogist*, *98*(10), 1870–1880. https://doi.org/10.2138/am.2013.4440

Schmidt, M. W., & Poli, S. (1998). Experimentally based water budgets for dehydrating slabs and consequences for arc magma generation. *Earth and Planetary Science Letters*, *163*(1-4), 361–379. https://doi.org/10.1016/S0012-821X(98)00142-3

Smyth, J. R., Frost, D. J., Nestola, F., Holl, C. M., & Bromiley, G. (2006). Olivine hydration in the deep upper mantle: Effects of temperature and silica activity. *Geophysical Research Letters*, *33*, L15301. https://doi.org/10.1029/2006GL026194

Sokol, A. G., Palyanov, Y. N., Kupriyanov, I. N., Litasov, K. D., & Polovinka, M. P. (2010). Effect of oxygen fugacity on the $H_2O$ storage capacity of forsterite in the carbon-saturated systems. *Geochimica et Cosmochimica Acta*, *74*(16), 4793–4806. https://doi.org/10.1016/j.gca.2010.05.032

Soustelle, V., Tommasi, A., Demouchy, S., & Ionov, D. A. (2010). Deformation and fluid-rock interaction in the supra-subduction mantle: Microstructures and water contents in peridotite xenoliths from the Avacha volcano, Kamchatka. *Journal of Petrology*, *51*(1-2), 363–394. https://doi.org/10.1093/petrology/egp085

Stalder, R., & Skogby, H. (2003). Hydrogen diffusion in natural and synthetic orthopyroxene. *Physics and Chemistry of Minerals*, *30*(1), 12–19. https://doi.org/10.1007/s00269-002-0285-z

Stalder, R., & Ulmer, P. (2001). Phase relations of a serpentine composition between 5 and 14 GPa: Significance of clinohumite and phase *E* as water carriers into the transition zone. *Contributions to Mineralogy and Petrology*, *140*(6), 670–679. https://doi.org/10.1007/s004100000208

Tielke, J. A., Zimmerman, M. E., & Kohlstedt, D. L. (2017). Hydrolytic weakening in olivine single crystals. *Journal of Geophysical Research*, *122*, 3465–3479.

Till, C. B., Grove, T. L., & Withers, A. C. (2012). The beginnings of hydrous mantle wedge melting. *Contributions to Mineralogy and Petrology*, *163*(4), 669–688. https://doi.org/10.1007/s00410-011-0692-6

Tollan, P. M. E., O'Neill, H. S. C., Hermann, J., Benedictus, A., & Arculus, R. J. (2015). Frozen melt–rock reaction in a peridotite xenolith from sub-arc mantle recorded by diffusion of trace elements and water in olivine. *Earth and Planetary Science Letters*, *422*, 169–181. https://doi.org/10.1016/j.epsl.2015.03.055

Tollan, P. M. E., Smith, R., O'Neill, H. S. C., & Hermann, J. (2017). Differences in the dependence of $H_2O$ concentration on the activity of $H_2O$ among the different substitution mechanisms of H in olivine: Implications for $H_2O$ storage in the upper mantle. *Progress in Earth and Planetary Science*, *4*(1), 14. https://doi.org/10.1186/s40645-017-0128-7

Tommasi, A., Langone, A., Padrón-Navarta, J. A., Zanetti, A., & Vauchez, A. (2017). Hydrous melts weaken the mantle, crystallization of pargasite and phlogopite does not: Insights from a petrostructural study of the Finero peridotites, southern Alps. *Earth and Planetary Science Letters*, *477*, 59–72.

Turner, M., Ireland, T., Hermann, J., Holden, P., Padrón-Navarta, J. A., Hauri, E. H., & Turner, S. (2015). Sensitive high resolution ion microprobe - stable isotope (SHRIMP-SI) analysis of water in silicate glasses and nominally anhydrous reference minerals. *Journal of Analytical Atomic Spectrometry*, *30*(8), 1706–1722. https://doi.org/10.1039/C5JA00047E

van Keken, P. E., Hacker, B. R., Syracuse, E. M., & Abers, G. A. (2011). Subduction factory: 4. Depth-dependent flux of $H_2O$ from subducting slabs worldwide. *Journal of Geophysical Research*, *116*, B01401

Walker, A. M., Hermann, J., Berry, A. J., & O'Neill, H. S. (2007). Three water sites in upper mantle olivine and the role of titanium in the water weakening mechanism. *Journal of Geophysical Research*, *112*, B05211. https://doi.org/10.1029/2006JB004620

Walter, M. J., Thomson, A. R., Wang, W., Lord, O. T., Ross, J., McMahon, S. C., … Kohn, S. C. (2015). The stability of hydrous silicates in Earth's lower mantle: Experimental constraints from the systems $MgO–SiO_2–H_2O$ and $MgO–Al_2O_3–SiO_2–H_2O$. *Chemical Geology*, *418*, 16–29. https://doi.org/10.1016/j.chemgeo.2015.05.001

Whitney, D. L., & Evans, B. W. (2010). Abbreviations for names of rock-forming minerals. *American Mineralogist*, *95*(1), 185–187.

Withers, A., & Hirschmann, M. (2008). Influence of temperature, composition, silica activity and oxygen fugacity on the $H_2O$ storage capacity of olivine at 8 GPa. *Contributions to Mineralogy and Petrology*, *156*(5), 595–605. https://doi.org/10.1007/s00410-008-0303-3

Withers, A. C., Bureau, H., Raepsaet, C., & Hirschmann, M. M. (2012). Calibration of infrared spectroscopy by elastic recoil detection analysis of H in synthetic olivine. *Chemical Geology*, *334*, 92–98. https://doi.org/10.1016/j.chemgeo.2012.10.002

Withers, A. C., & Hirschmann, M. M. (2007). $H_2O$ storage capacity of $MgSiO_3$ clinoenstatite at 8–13 GPa, 1,100–1,400°C. *Contributions to Mineralogy and Petrology*, *154*(6), 663–674. https://doi.org/10.1007/s00410-007-0215-7

Withers, A. C., Hirschmann, M. M., & Tenner, T. J. (2011). The effect of Fe on olivine $H_2O$ storage capacity: Consequences for $H_2O$ in the Martian mantle. *American Mineralogist*, *96*(7), 1039–1053. https://doi.org/10.2138/am.2011.3669